applied sciences

MDPI

Article

Towards the Development of a Z-Scheme FeOx/g-C_3N_4 Thin Film and Perspectives for Ciprofloxacin Visible Light-Driven Photocatalytic Degradation

Murilo Fendrich [1], Om Prakash Bajpai [1], Raju Edla [1], Alessandra Molinari [2], Paola Ragonese [3], Chiara Maurizio [3], Michele Orlandi [1] and Antonio Miotello [1,*]

[1] Physics Department, University of Trento, Via Sommarive 14, 38123 Trento, Italy; murilo.fendrich@unitn.it (M.F.); michele.orlandi@unitn.it (M.O.)
[2] Department of Chemical, Pharmaceutical and Agricultural Sciences, University of Ferrara, Via L. Borsari 46, 44121 Ferrara, Italy
[3] Physics and Astronomy Department and CNISM, University of Padova, Via Marzolo 8, 35131 Padova, Italy
* Correspondence: antonio.miotello@unitn.it

Abstract: Thermally synthesized graphitic carbon nitride (g-C_3N_4) over pulsed laser deposition (PLD) produced urchin-like iron oxide (FeOx) thin films were fabricated via in situ and ex situ processes. Materials characterisation revealed the formation of the graphitic allotrope of C_3N_4 and a bandgap E_g for the combined FeOx/g-C_3N_4 of 1.87 and 1.95 eV for each of the different fabrication strategies. The in situ method permitted to develop a novel petal-like morphology, whereas for the ex situ method, a morphological mixture between FeOx bulk and g-C3N4 was observed. Given the improved optical and morphological properties of the in situ film, it was employed as a proof of concept for the direct photocatalysis and photo-Fenton removal of ciprofloxacin antibiotic (CIP) under visible light irradiation. Improved photocatalytic activity (rate constant $k = 8.28 \times 10^{-4}$ min^{-1}) was observed, with further enhancement under photo-Fenton conditions ($k = 2.6 \times 10^{-3}$ min^{-1}), in comparison with FeOx + H_2O_2 ($k = 1.6 \times 10^{-3} min^{-1}$) and H_2O_2 only ($k = 1.3 \times 10^{-4}$ min^{-1}). These effects demonstrate the in situ methodology as a viable route to obtain working heterojunctions for solar photocatalysis in thin-film materials, rather than the more common powder materials.

Keywords: FeOx/g-C_3N_4 thin films; petal-like morphologies; Z-scheme; visible light photocatalysis; ciprofloxacin degradation

Citation: Fendrich, M.; Bajpai, O.P.; Edla, R.; Molinari, A.; Ragonese, P.; Maurizio, C.; Orlandi, M.; Miotello, A. Towards the Development of a Z-Scheme FeOx/g-C_3N_4 Thin Film and Perspectives for Ciprofloxacin Visible-Light Driven Photocatalytic Degradation. *Appl. Sci.* **2023**, *13*, 10591. https://doi.org/10.3390/app131910591

Academic Editors: Hicham Idriss and Hyungjun Kim

Received: 27 July 2023
Revised: 25 August 2023
Accepted: 19 September 2023
Published: 22 September 2023

1. Introduction

Direct Z-scheme photocatalysis mechanisms, obtained by combining two different photocatalysts (PC), have been proven to be a promising option for enhancing photocatalytic reactions efficiency [1].

In this configuration, inspired by the study of natural photosynthesis, photogenerated electrons in the conduction band (CB) of a PC I can recombine with photogenerated holes in the valence band (VB) of a PC II: this results in a charge-separated state where holes are left on the VB of PC I and electrons on the CB of PC II, separated in space. This inhibits recombination, thus enhancing lifetimes and boosting the yield of redox processes employing them. Z-schemes can be implemented using two semiconductors with opportunely aligned band edges and offers the possibility of using materials with different bandgaps, with a double advantage: (1) materials that are good oxidants but poor reductants can be used as PC I and the reverse can be used for PC II, thus maximizing the activity of their redox potentials; and (2) a broader portion of sunlight spectrum can be exploited.

For these reasons, Z-schemes are increasingly popular in photoactive materials and are increasingly studied for a variety of applications, from water splitting to wastewater remediation [2,3].

Graphitic carbon nitride (g-C_3N_4)-based materials recently attracted great attention due to, among other things, useful optical properties, high chemical stability, and ease of fabrication [4]. g-C_3N_4-based materials could also be used as Fenton-like catalysts, adsorbents, disinfectants, and membrane materials [5–7]. Despite these advantages, g-C_3N_4 also has significant drawbacks, such as poor UV–visible absorption (<450 nm), low surface area, and fast recombination kinetics for photogenerated electron–hole couples, limiting its photocatalytic performance.

Different methodologies for modifying g-C_3N_4 have been investigated in order to improve its performance, for example by doping g-C_3N_4 with different elements: TiO_2 [8–12], Cu [13], SiC [14], Ag [15,16], ZnO [17], graphitized polyacrylonitrile [18], CdO [19], and WO_3 [20]. However, most of these dopings comprise nanomaterials in powdered form and are used for colloidal photocatalysis.

Much less investigated is the possibility of utilizing g-C_3N_4 (either alone or in composites) as thin films over substrate surfaces, for example FTO [21–24]. In water purification applications, the use of colloidal suspensions still represents the main research field due the available high surface areas. However, the recovery of the material, after use, constitutes an additional problem [25]. From an industrial perspective, working with immobilized photocatalysts, such as thin films, allows the facile removal at the end of the process and displays enhanced compatibility with flow reactor installations [26,27]. On the other hand, the application of Z-schemes or other useful heterojunction-based design principles is quite straightforward and well established for nanopowders but much more difficult for thin-films. Indeed, for such a material to be effective in photocatalysis, both the components need to have a solid–liquid interface at which redox reactions with substrates can occur, and this is not possible with the layered composites generally obtained with most thin-film fabrication methods.

In photocatalysis, g-C_3N_4 composites have been recently investigated for the degradation of emerging pharmaceutical contaminants (like sulphonamides, acyclovir) as well as of pesticides [28–33]. Only a few papers deal with the synthesis of FeOx/C_3N_4 composites for oxidation processes, water splitting, electro-catalysis, dye degradation, or artificial photosynthesis [34–36]. Note that both materials are industrially scalable, economically viable, abundant (in the case of iron oxides), and environmentally compatible [37], so that a composite, based on these materials, which incorporates heterojunction effects into a thin-film design would be a breakthrough towards application. Regarding pharmaceutical contaminants specifically, CIP, a fluoroquinolone antibiotic used in medicine and veterinary practice both, is of particular interest: it is one of the most widely used antibiotics worldwide and standard wastewater treatments are largely ineffective for its removal, leading to its frequent detection in surface waters in many regions. It is thus considered a potential source of antimicrobial resistance (AMR), an increasingly severe threat to public health [38]. Note that, while the final target of solar-wastewater treatments is generally the complete removal of pollutants via mineralisation, avoiding AMR in principle only requires the inactivation of antibiotic residues in water instead [39]. To this end, solar-driven photocatalysis would be a potentially cost-effective, high-efficiency treatment process.

In this paper, we investigate the production of Z-scheme composite thin films based on the combination of pulsed laser deposition (PLD)-produced urchin-like iron oxide (FeOx) nanostructured film with g-C_3N_4 to be employed for ciprofloxacin (CIP) degradation. The urchin-like FeOx was recently developed in our lab and has been selected as a platform for the composite synthesis because it has good solar spectrum compatibility, with an energy bandgap E_g = 2.2 eV; consists of hierarchical structures, which are beneficial for applications requiring high surface area [40,41]; and finally, it is photo-Fenton active [42,43]. Two different strategies were used to prepare FeOx/g-C_3N_4

composite films. In the first case, we grew the petal-like g-C_3N_4 over iron urchins by directly drop-casting the melamine solution followed by thermal treatment (in situ). In the second case, previously synthesized g-C_3N_4 powder was spin-coated over iron urchins (ex situ). The photocatalytic performance of the coatings has been evaluated via the degradation of ciprofloxacin (CIP) under visible light. CIP is indeed an important emerging contaminant, but at the same time it is well-studied, its degradation mechanism well reported, and it can easily be followed by simple UV–visible methods; therefore, it can be used to evaluate and tune the performances of our new materials [44–49].

2. Materials and Methods

2.1. Materials and Reagents

Starting elements were metallic iron powder (Ventron GmBh (Karlsruhe, Germany), purity 97%, particle size mesh 325, 56 g/mol), boric acid (H_3BO_3 Sigma-Aldrich (St. Louis, MO, USA) BioXtra, purity > 99.5%, 61.83 g/mol), and melamine (C3H6N6, Sigma-Aldrich, purity > 99%, 126.12 g/mol). Ethanol absolute (VWR, purity 97%, 46.08 g/mol) was used as a dispersing agent for melamine and synthesized g-C_3N_4 powder. Ciprofloxacin ($C_{17}H_{18}FN_3O_3$, Standard PHR1044 Sigma-Aldrich, purity 99%, 385.82 g/mol) was employed to test the efficiency of photocatalysis. H_2O_2 solution (Merck (Rahway, NJ, USA), EMSURE ISO, concentration 30%, 34.01 g/mol) was employed in the photo-Fenton reactions.

2.2. Synthesis of Iron Oxide Urchins

Urchin-like FeOx nanostructured thin films were produced via PLD following the protocol and apparatus published elsewhere [40,50]. Briefly, the films were obtained using a KrF Lambda Physik excimer laser with a 248 nm wavelength, 25 ns pulse duration, and 20 Hz repetition rate. Targets were prepared as pellets of cold-pressed iron and H_3BO_3-mixed powders (1:1 weight). The deposition of films was carried out on both Si slides (for the purpose of characterisation) and glass slides (75 mm × 26 mm) in O_2 atmosphere (4.5 Pa) at room temperature by keeping them at distance of 4.5 cm from the target. During the deposition, a laser fluence of 3 J/cm^2 was applied using optical focusing, and 10,000 laser pulses were used for each single substrate glass slide. The prepared films were thermally annealed at 550 °C for 4 h in air atmosphere with a heating rate of 5 °C/min. Deposited films weight was measured using a balance with 10^{-5} g resolution.

2.3. Synthesis of g-C_3N_4 Powder

Melamine was used as the precursor for g-C_3N_4 synthesis. A total of 10 g of melamine powder was added into a porcelain crucible (200 mL) with a closed cap. Before the synthesis, the porcelain crucible was well polished with an abrasive sheet. In the synthesis process, the crucible containing melamine was heated inside a muffle furnace at 550 °C for 4 h with the heating rate of 9 °C/min [51]. This protocol was used to produce bulk g-C_3N_4 powder for characterisation and as part of the process to produce ex situ film.

2.4. Preparation of FeOx/g-C_3N_4 Composite Thin Films

The FeOx/g-C_3N_4 composite materials were prepared by employing the iron oxide urchin film described in Section 2.2 as a support for the g-C_3N_4, following two distinct procedures as described below and schematically presented in Figure 1:

(a) The g-C_3N_4 powder was synthesized ex situ by thermally heating melamine for 4 h (protocol from Section 2.3). The synthesized g-C_3N_4 was dispersed in ethanol with concentration of 40 mg/mL. The prepared suspension was spin-coated on top of the iron urchins with a rotational speed of 800 rpm for 60 s. The composite material was dried at 60 °C for 4 h to evaporate the extra solvent. The final composite sample is referred to from here onwards as (FeOx/g-C_3N_4)*ex.*

(b) Starting from melamine, g-C_3N_4 was synthesized in situ on the surface of iron oxide urchin. Specifically, the melamine powder was dispersed in ethanol with a concentration of 100 mg/mL. The prepared suspension was used to spread a controlled amount of melamine precursor on top of the iron urchin film via the drop-casting method. Subsequently, films were heated in a muffle furnace at 550 °C for 1 h to obtain the g-C_3N_4 on top of the iron oxide urchins. The prepared composite is referred to from here onwards as (FeOx/g-C_3N_4)*in*.

Here, we selected 4 h and 1 h durations of annealing for ex situ and in situ methods, respectively, based on the optimisation described in the Supplementary Materials (Section S1).

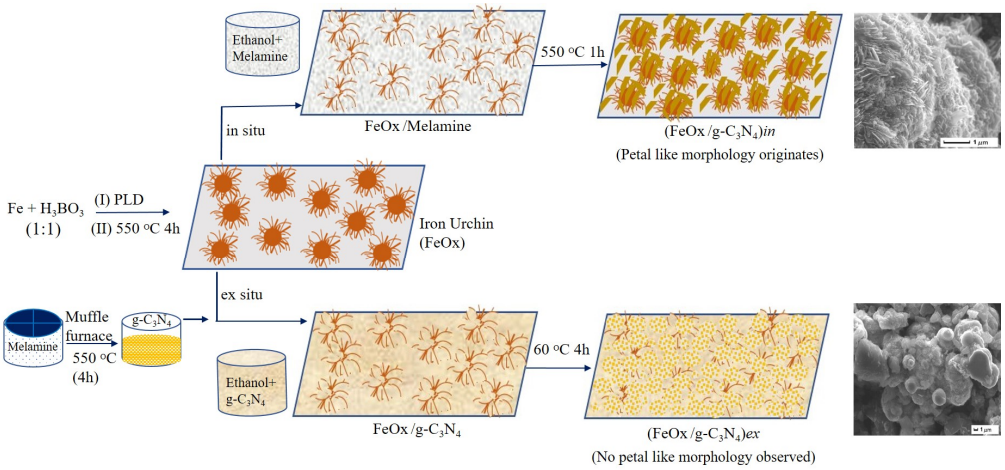

Figure 1. Schematic showing the synthesis of iron urchin (FeOx), g-C_3N_4, and FeOx/g-C_3N_4 composites via different procedures.

2.5. Materials Characterisation

The properties of the obtained materials were investigated via different characterisation techniques. A LabRAM Aramis Jobin-Yvon Horiba μ-Raman equipped with a He-Ne laser source (785 nm) was used for Raman spectroscopy measurements. FT-IR was performed using a JASCO model 4600 instrument (Easton, PA, USA). Grazing incidence XRD (GIXRD) was employed to analyse the crystallinity of samples using a X'Pert Pro diffractometer, working with the Cu Kα radiation. A field emission scanning electron microscope (FEG-SEM, JSM-7001F, JEOL (Tokyo, Japan)) equipped with an Energy-Dispersive X-ray Spectroscopy (EDXS-INCA PentaFETx3, Oxford Instruments (Abingdon, UK)) analyser was used to examine morphology and composition, whereas TEM analysis was performed in order to add structural information at a microscopic scale (S/TEM TALOS F200S, ThermoFisher, Waltham, MA, USA). UV and visible (UV–Vis) absorption spectra were measured using a VARIAN Cary 5000 UV-Vis-NIR spectrophotometer over a wavelength range of 200 to 800 nm. The Kubelka–Munk function (Equation (1)) and the Tauc equation were used to evaluate the direct bandgap of the synthesized materials:

$$F(R) = \frac{(1-R)^2}{2R} \quad (1)$$

where R is the reflectance of the sample.

The Tauc equation for direct electronic transitions is described in Equation (2):

$$(\alpha h\nu)^2 = A(h\nu - E_g) \quad (1)$$

where α is the optical absorption coefficient; $h\nu$ is the incident photon energy in eV; A is the material-dependent absorption constant; and Eg is the energy bandgap.

X-ray photoemission spectroscopy (XPS) measurements were performed on the thin film coatings to understand the surface chemical states of the elements. The X-ray source was a monochromatized Al Kα (1486.6 eV) source, and the spectra were collected from an electrostatic hemispherical electron energy analyser with ±8° of acceptance angle. The X-ray beam incidence was at an angle of 45° on the surface of the samples and all spectra were acquired in normal emission conditions with an initial base pressure of 2×10^{-9} mbar. The calibration of the data was performed using the C 1 s native peak present on the surface of the samples.

2.6. Photocatalysis Experiments: Degradation of Ciprofloxacin

In a typical experiment, the photocatalyst film was positioned in the centre of a borosilicate glass beaker and immersed in an aqueous solution (50 mL) containing CIP (C_0 = 10 ppm) on. The beaker was covered with aluminium foil and kept in the dark for 30 min while stirring (150 rpm) to achieve adsorption–desorption equilibrium. After 30 min of initial dark, the foil was removed and the beaker was irradiated for 180 min. When required, H_2O_2 was added to the starting solution to reach a (5×10^{-4} M) concentration. Aliquots (1 mL) of irradiated solution were taken at fixed time intervals and UV–Vis spectra were recorded to evaluate the extent of CIP disappearance. The absorbance values at λ_{max} = 272 nm were collected and the degradation of CIP was reported as:

$$\text{Degradation efficiency (\%)} = \left(\frac{C_o - C_t}{C_o}\right) \times 100 = \left(\frac{A_o - A_t}{A_o}\right) \times 100 \quad (2)$$

where C_o and A_o are the starting molar concentration and absorbance of CIP while C_t and A_t are the molar concentration and absorbance of CIP at time t. Control experiments were carried out by irradiating the starting solution of CIP in the absence of any photocatalyst.

The irradiation was provided by three halogen lamps (Osram (Berlin, Germany) HALOPAR 30, 75W, 30° aperture angle, luminous flux of 350 lumens) positioned in a vertical support at 40 cm height from the reactor, and they were slightly inclined to direct the focus towards the centre of the beaker containing the catalyst and the CIP solution. The spectral irradiance of the light source is reported in Figure S1. Cooling was provided by adding a constant supply of ice around the reactor with a monitored temperature (35–20 °C). UV–Visible absorption spectra were recorded using a VARIAN Cary 5000 UV–Vis–NIR spectrophotometer. When working in photo-Fenton mode, a 5×10^{-4} M of H_2O_2 is employed, which is high enough to ensure a large excess (ca. 20 times with respect to the 2.59×10^{-5} M CIP) and low enough for the absorbance of H_2O_2 not to interfere with the spectrophotometric determination of CIP.

3. Results and Discussion

3.1. g-C_3N_4 Characterisation

Synthesized g-C_3N_4 powder and melamine precursor were characterized in terms of structure and morphology (Supplementary Materials, Figures S2–S7). A UV–Vis spectrum was acquired to characterize the melamine precursor before synthesis to g-C_3N_4, and the spectrum shows significant absorbance only in the UV region (<275 nm), as seen in Figure S2. After the melamine synthesis, a powder-like morphology with agglomerated particles under 100 nm in size was observed in the SEM analysis, and the presence of only C and N elements was confirmed from corresponding EDXS spectra (Figure S3). In the FTIR (Figure S4), the peaks that appear in the 1200–1700 cm^{-1} region are related to the stretching modes of C=N and C–N hetero-cycles, and the peaks at 875 and 804 cm^{-1} indicate the presence of the stretching mode of the triazine ring [51]. Micro-Raman analysis proves the presence of g-C_3N_4 from the peaks at 211, 359, 471, 588, 706, 768, 984, 1117, 1151, 1232, and 1312 cm^{-1}, respectively (Figure S5 and Table S1). Also, the peaks 1360 cm^{-1} (D band) and 1580 cm^{-1} (G band) confirm the formation of C–N [52,53]. XRD analysis further confirmed

the presence of the graphitic-like phase of C_3N_4 lattice system given by the (002) peak (Figure S6). An increase in UV absorbance was observed in the 400–500 nm range with a maximum at 400 nm, and the Tauc plot demonstrates that the direct bandgap of the synthesized g-C_3N_4 powder is 2.92 eV (Figure S7).

3.2. FeOx/g-C_3N_4 Composite Characterisation

Figure 2 presents the FTIR spectra comparison between the FeOx iron urchins film only, (FeOx/g-C_3N_4)*in* and (FeOx/g-C_3N_4)*ex* composites. Both the composite materials present the C-N and C=N vibration states in the wavenumbers range between 1200 and 1700 cm^{-1}. A triazine peak is also observed at 804 cm^{-1}. Sharper peak formation in the mentioned range is more evident in the (FeOx/g-C_3N_4)*ex* composite in comparison to (FeOx/g-C_3N_4)*in*. This can possibly be attributed to the higher mass of g-C_3N_4 on top of the FeOx supporting material. The corresponding FeOx spectrum involves the unresolved peaks below 1000 cm^{-1}, which are related to Fe-O stretching vibrations [54]. In Figure 2, a cluster of weak bands found at around 1500 cm^{-1} correspond to the vibration modes of carbonates resulting from interaction of the surface with CO_2 from the air. This is commonly observed in iron oxide surfaces exposed to air humidity, which leads to the formation of hydroxides that are, in turn, susceptible to carbonate formation [55].

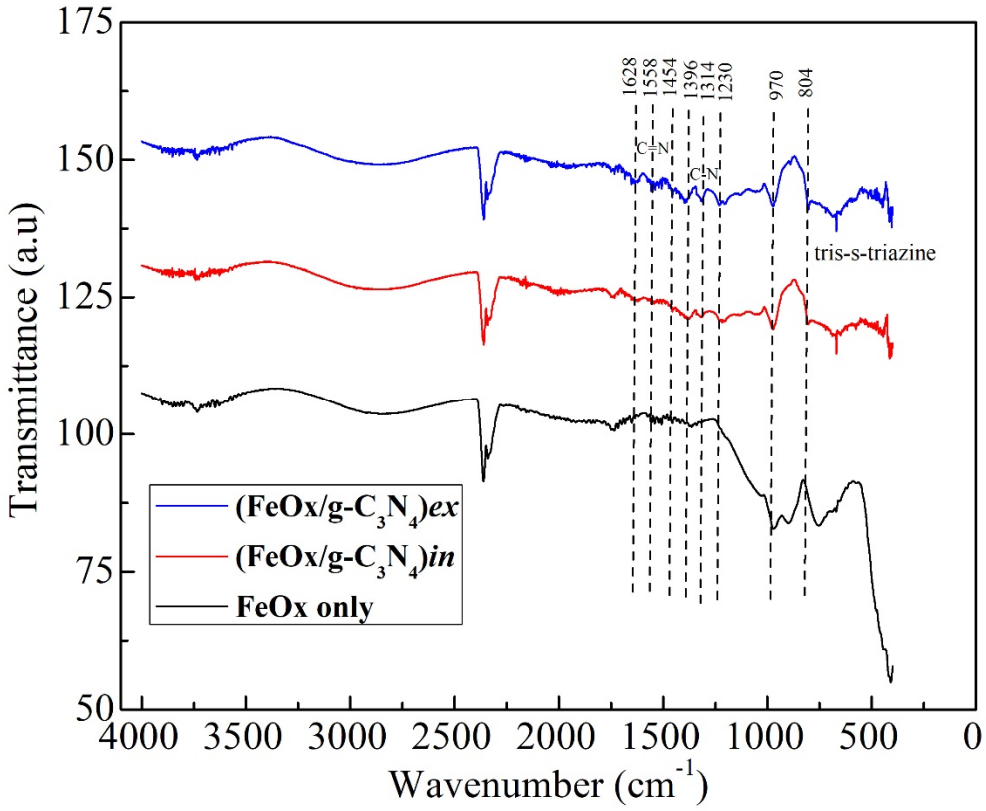

Figure 2. FTIR spectra comparisons between FeOx and the composites FeOx/g-C_3N_4.

Micro-Raman analysis was also employed to investigate the properties of the (FeOx/g-C_3N_4)*in* and (FeOx/g-C_3N_4)*ex* as well as the reference FeOx support material. The Raman spectra (Figure 3) show the peaks of g-C_3N_4 identified at 211, 359, 471, 588, 706, 768, 984, 1117, 1151, 1232, and 1312 cm^{-1}, respectively. For the (FeOx/g-C_3N_4)*ex*, spectrum shows essentially the g-C_3N_4 bulk nature due to the complete coverage of the FeOx thin film. The (FeOx/g-C_3N_4)*in* spectrum presents the g-C_3N_4 with the characteristic peaks shifted with respect to the bulk powder g-C_3N_4, such as the 521, 749, 810, 999, 1156, 1266, and 1346 cm^{-1} and small traces of FeOx at 298 and 1386 cm^{-1} being the other peaks in

overlap with g-C_3N_4. The shifting on the FeO_x/g-C_3N_4 (in situ) sample is attributed to the atomic lattice compressive stress because of synthesis procedure. In particular, in situ synthesis induces stress modifications on the FeOx because of the melamine thermal conversion to C3N4 on its surface that indeed favours strong adhesion with the substrate. On the other hand, in the ex situ preparation condition, the interaction between the already prepared g-C3N4 powder and the FeOx surface is milder, as proved by the poor adhesion [56]. Peaks assignments are presented in Supplementary Table S1.

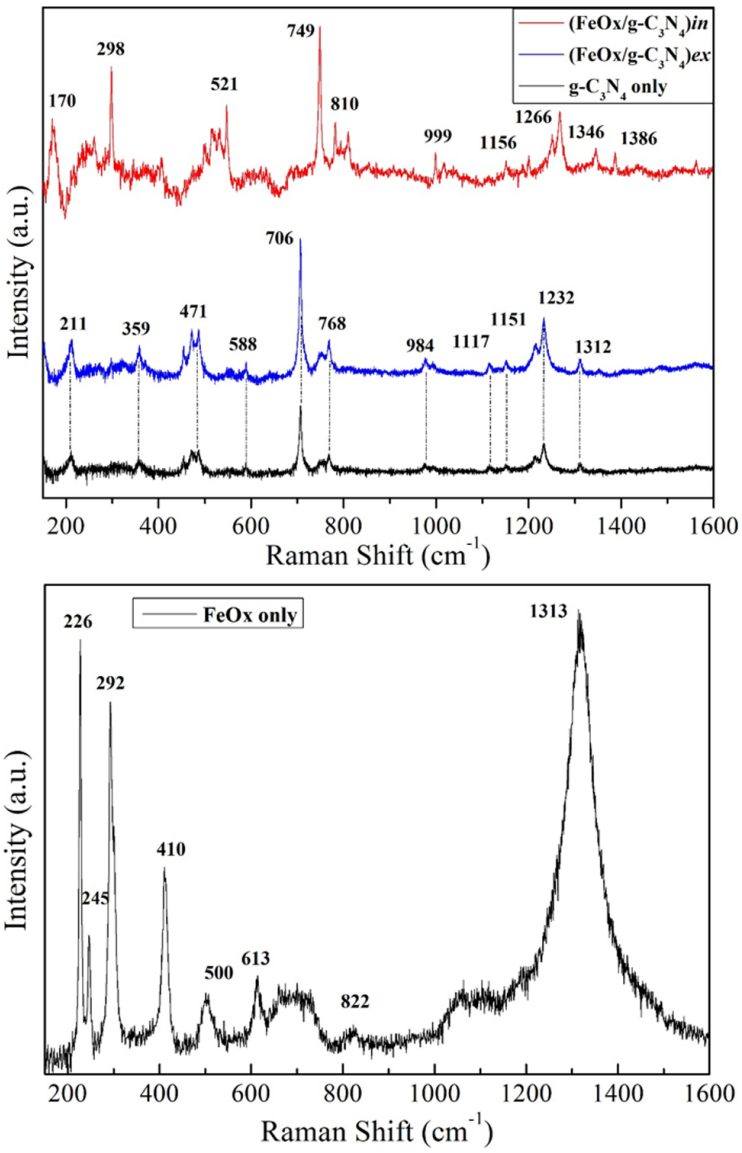

Figure 3. Raman spectra of g-C_3N_4 compared to composites (FeOx/g-C_3N_4)*in* and (FeOx/g-C_3N_4)*ex* (**a**) and FeOx supporting material (**b**).

Figure 4 presents the GIXRD patterns for both (FeOx/g-C_3N_4)*in* and (FeOx/g-C_3N_4)*ex*. (FeOx/g-C_3N_4)*ex* clearly presents the peaks at 13.1° and 27.5° corresponding to the (100) and (002) crystal planes of the g-C_3N_4 (JCPDS No. 87-1526). The diffraction peaks typical of hematite are labelled (012), (104), (113), (024), (116), and (122) (JCPDS No. 33-0664), and the observed traces of magnetite phase are labelled (111), (220), (311), (222), and (400) (JCPDS No. 19-0629). According to the growth mechanism of the urchins during the oxidizing annealing, the most oxidized iron phase (Fe_2O_3) is expected to most likely be present on the surface of the nanostructured film, in contact with the solution and with the g-C_3N_4.

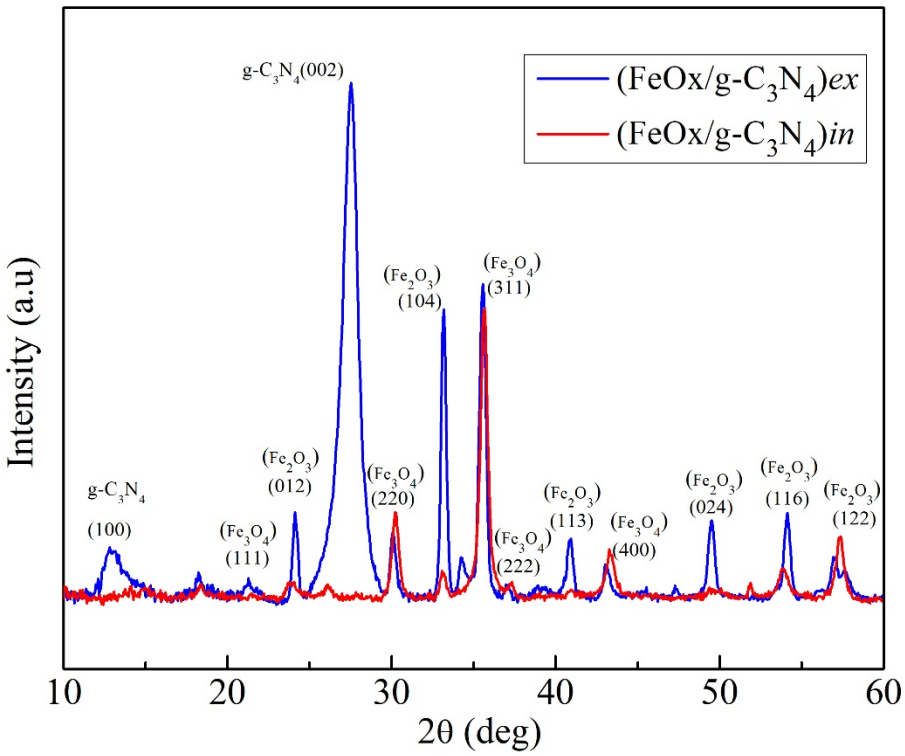

Figure 4. GIXRD patterns for the films (FeOx/g-C_3N_4)*in* and (FeOx/g-C_3N_4)*ex* recorded at incidence angle = 0.5 deg.

On the other hand, in the (FeOx/g-C_3N_4)*in* there is clear evidence of hematite and traces of magnetite. However, in comparison to (FeOx/g-C_3N_4)*ex*, the (002) peak of g-C_3N_4 is observed slightly shifted toward lower diffraction angle with considerably reduced intensity and also the (100) peak is apparently supressed. This suggests the intercalation of the layered structure of g-C_3N_4 by the abundant urchin-like structures (size ~10–20 nm) present on the surface of FeOx contributing to diminish the peak [57,58]. According to the Bragg equation ($\lambda = 2d\sin\theta$), the expanded interlayer distance of the d-spacing due to the intercalation of iron urchins into g-C_3N_4 layers may lead to the shift of the diffraction peak toward low angle. Moreover, the reduced intensity of the peak shows the possibility of less dense lamellar structure of the g-C_3N_4 in the composite due to the presence of small amounts of g-C_3N_4 (in the form of thin petals) on the FeOx surface [59,60]. These structural changes likely imply that in the in situ method of the formation of composite films, the g-C_3N_4 interacts and reconfigures the surface of FeOx differently than ex situ method.

The absorption spectra and Tauc plot of the FeOx/g-C_3N_4 composites are presented in Figure 5. An absorption region can be observed from the visible range (<600 nm) while a constant increase up to the UV range of the spectrum is detected for both composite materials. Interestingly, the (FeOx/g-C_3N_4)*in* composite film shows lower bandgap (~1.87 eV) than the (FeOx/g-C_3N_4)*ex* composite (~1.95 eV). Also, the observed bandgaps (1.87 and 1.95 eV) are in agreement with the literature [61]. For both synthesis methods, due to the presence of FeOx as the supporting material, the absorbance is shifted towards the visible part of the spectrum in comparison to the bulk g-C_3N_4 presented in Figure S7.

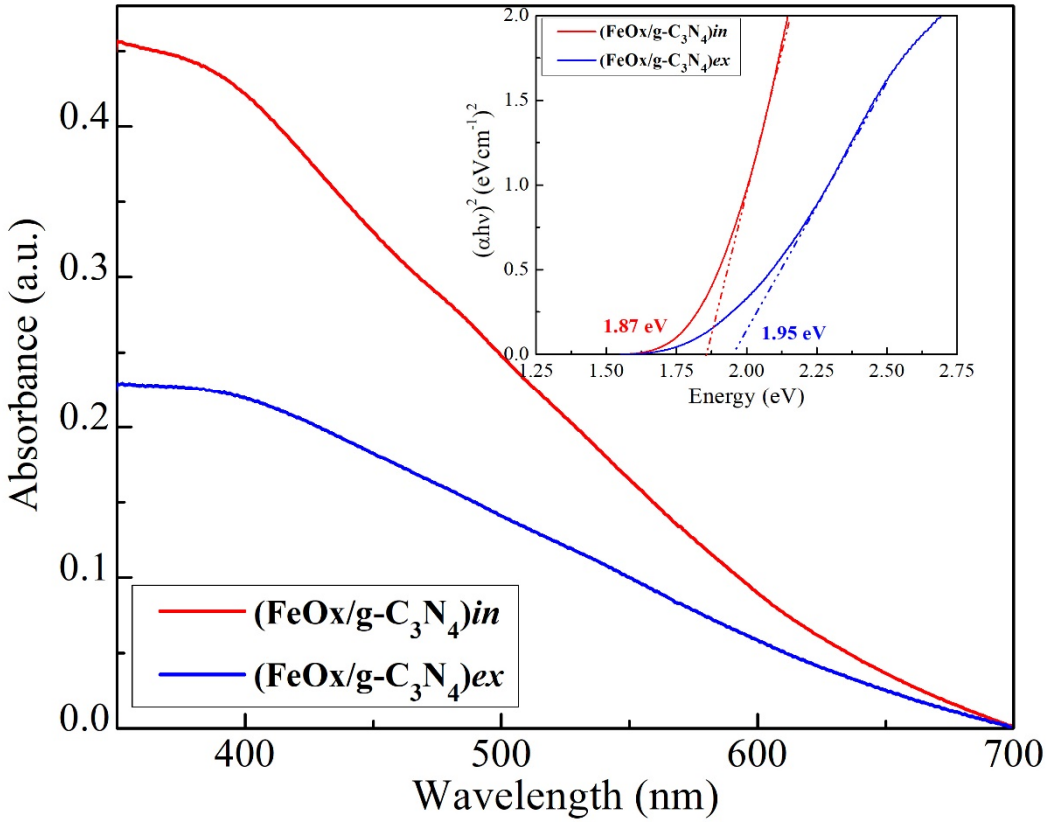

Figure 5. UV–Vis absorption spectra and corresponding Tauc plot (inset) of the synthesized (FeOx/g-C_3N_4)*in* and (FeOx/g-C_3N_4)*ex* composites materials.

Morphology and composition of the synthesized FeOx iron urchins and of the composites (FeOx/g-C_3N_4)*in* and (FeOx/g-C_3N_4)*ex* FeOx were investigated using SEM and EDXS techniques. Figure 6 presents the images of the surface of the FeOx urchin-like structure produced by PLD and annealed at 550 °C for 4 h in a tubular furnace used as the support material. EDXS results essentially confirm the presence of Fe and O on the microstructures (Figure S8). This agrees with previously published reports on this material [40,42]. The mass of the FeOx films was 21 ± 2 mg before the composite preparation steps.

SEM images in Figure 7 show the morphology of the (FeOx/g-C_3N_4)*in* composite. The formation of a petal-like microstructure (Figure 7a,b) is now observed as compared to the bare FeOx urchin. From Figure 7c, it is also observable that urchins present on the FeOx surface possibly intercalate the petal structure. A special formation of petal-like morphology growth is highlighted in (Figure 7d) as a single petal close-up (magnified image in the inset). Moreover, EDXS (Figure S9) confirms the presence of the C, N, Fe, and O elements in the composite film. The mass of the composite is about 10 mg more than the 21 ± 2 mg of the initial FeOx. This corresponds to 5–10% conversion yield of melamine.

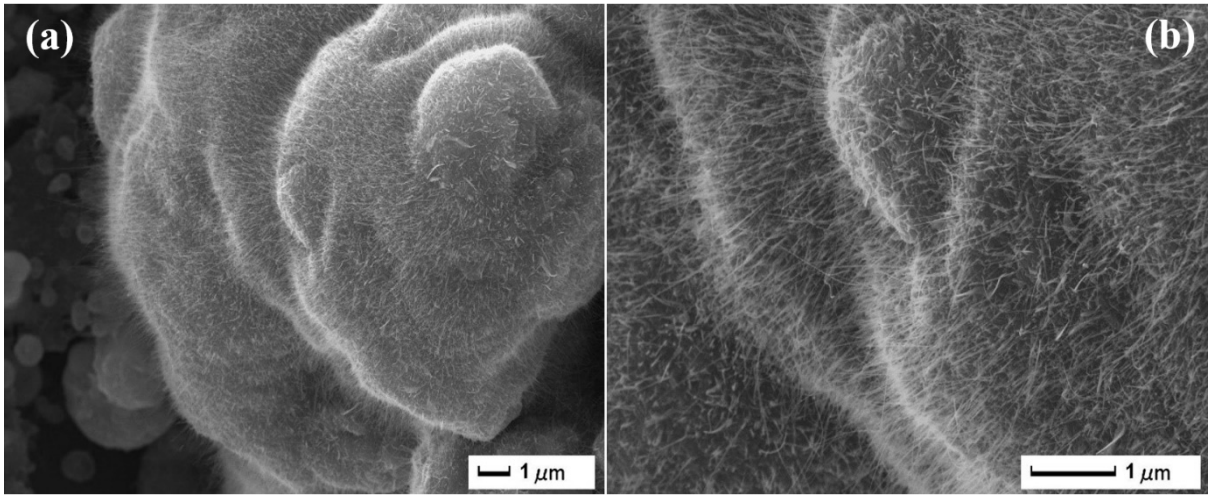

Figure 6. SEM images (**a**,**b**) showing the bare surface of the FeOx urchin-like structures employed in the composite with g-C_3N_4.

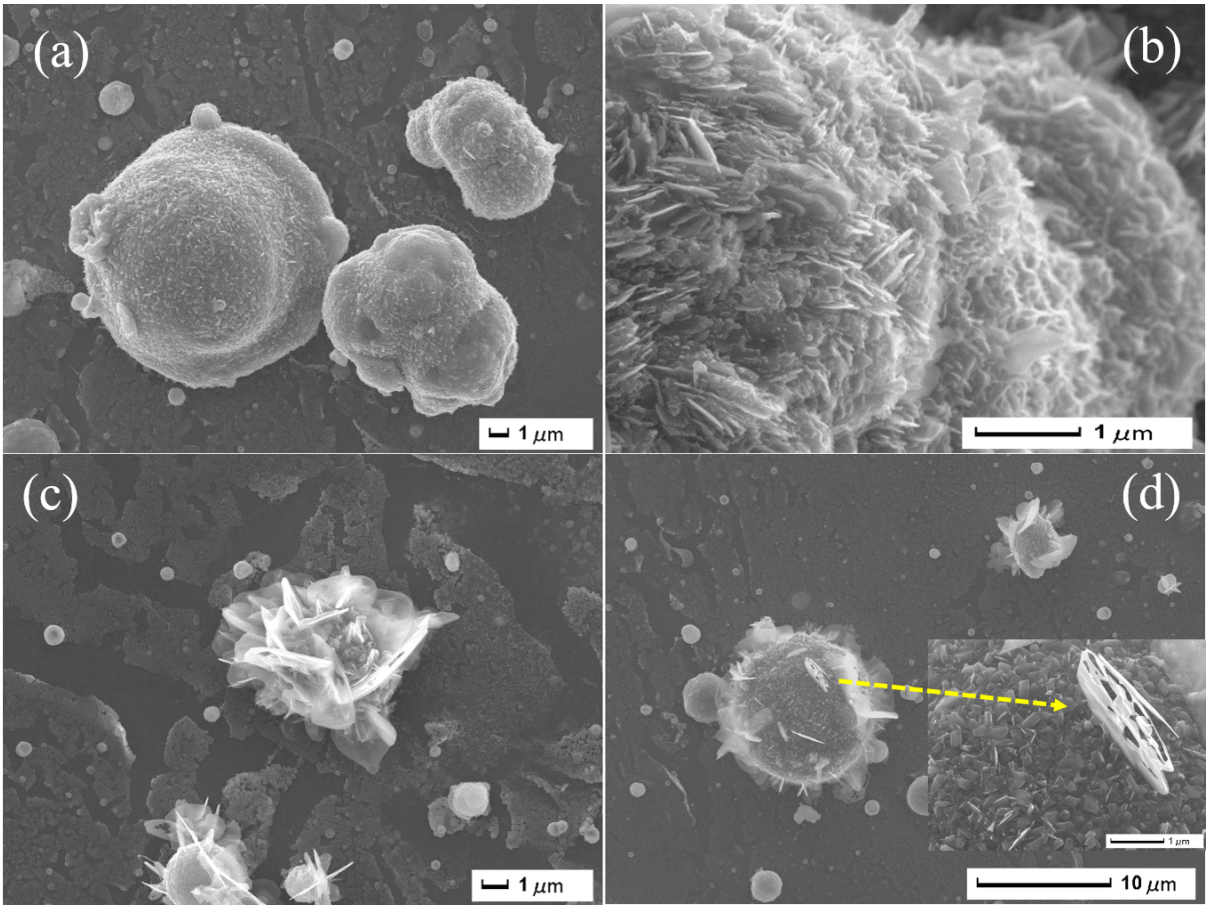

Figure 7. SEM images (**a**–**d**) of (FeOx/g-C_3N_4)*in* composite thin films.

Morphology of the synthesized composite (FeOx/g-C_3N_4)*ex* are presented in Figure 8a–c. The visual inspection of the images demonstrates the absence of petal-like morphology and island separation (Figure 8d) between the FeOx particles and g-C_3N_4 deposited on the surface of the iron urchins. In this case, the mass increase was about 40 mg (about 60 mg total composite mass), due to the drying of 1mL solution after the spin-coating process. EDXS (Figure S10) confirms the distinct separation of particles in the composite materials.

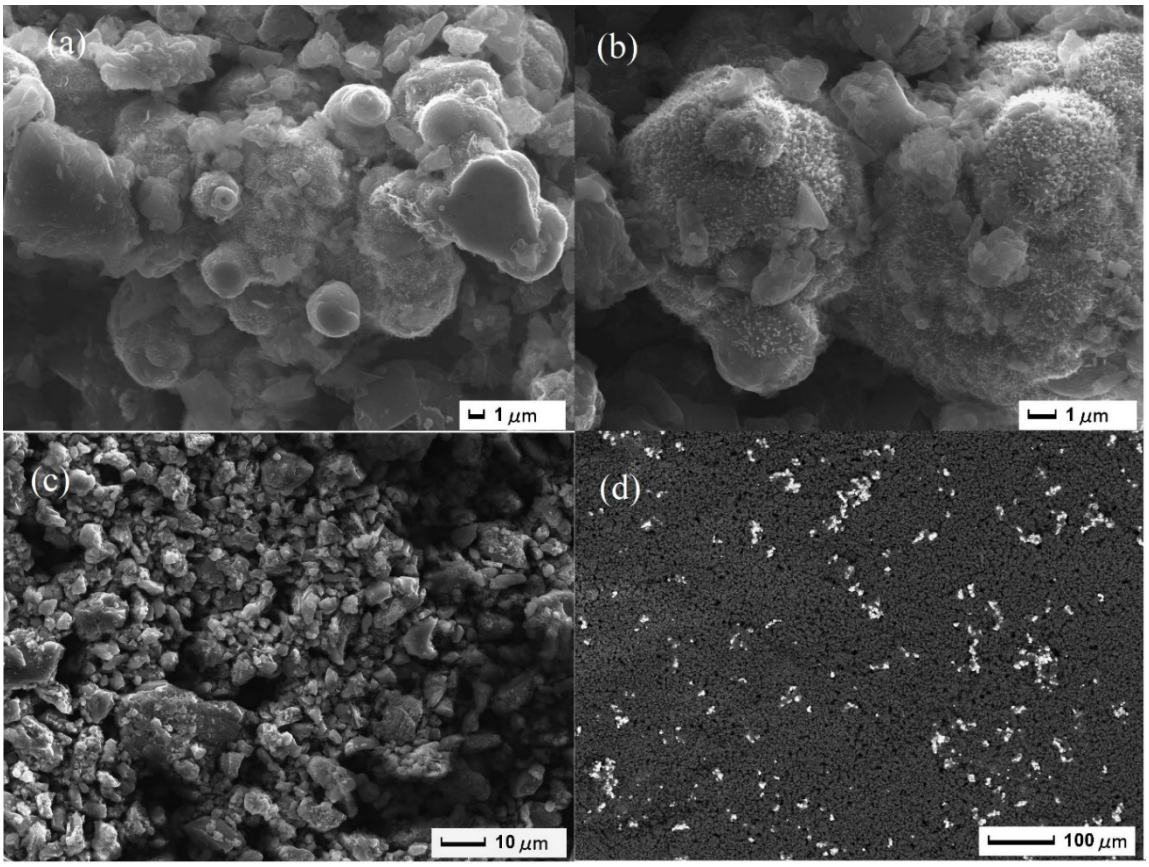

Figure 8. SEM images (**a**–**d**) of (FeOx/g-C_3N_4)*ex* composite thin films.

The morphology, composition, and crystalline structures of the composite (FeOx/g-C_3N_4)*in* were also investigated using HRTEM. Figure 9a–c presents the image of a single petal partially covered by g-C_3N_4 (darker areas). The magnification of figure 9a shows lattice fringes 0.252 and 0.295 nm and the white arrowheads define intervals corresponding to 10 lattice planes. The SAED spectra of clean single crystal return hematite or magnetite spot diffraction patterns (Figure S11), whereas larger area SAED spectra containing crystalline structure and darker regions show the presence of both Fe_2O_3 and Fe_3O_4 as well as the (002) peak of g-C_3N_4, which supports the XRD results (SAED patterns were identified with the identical XRD JCPDS card database).

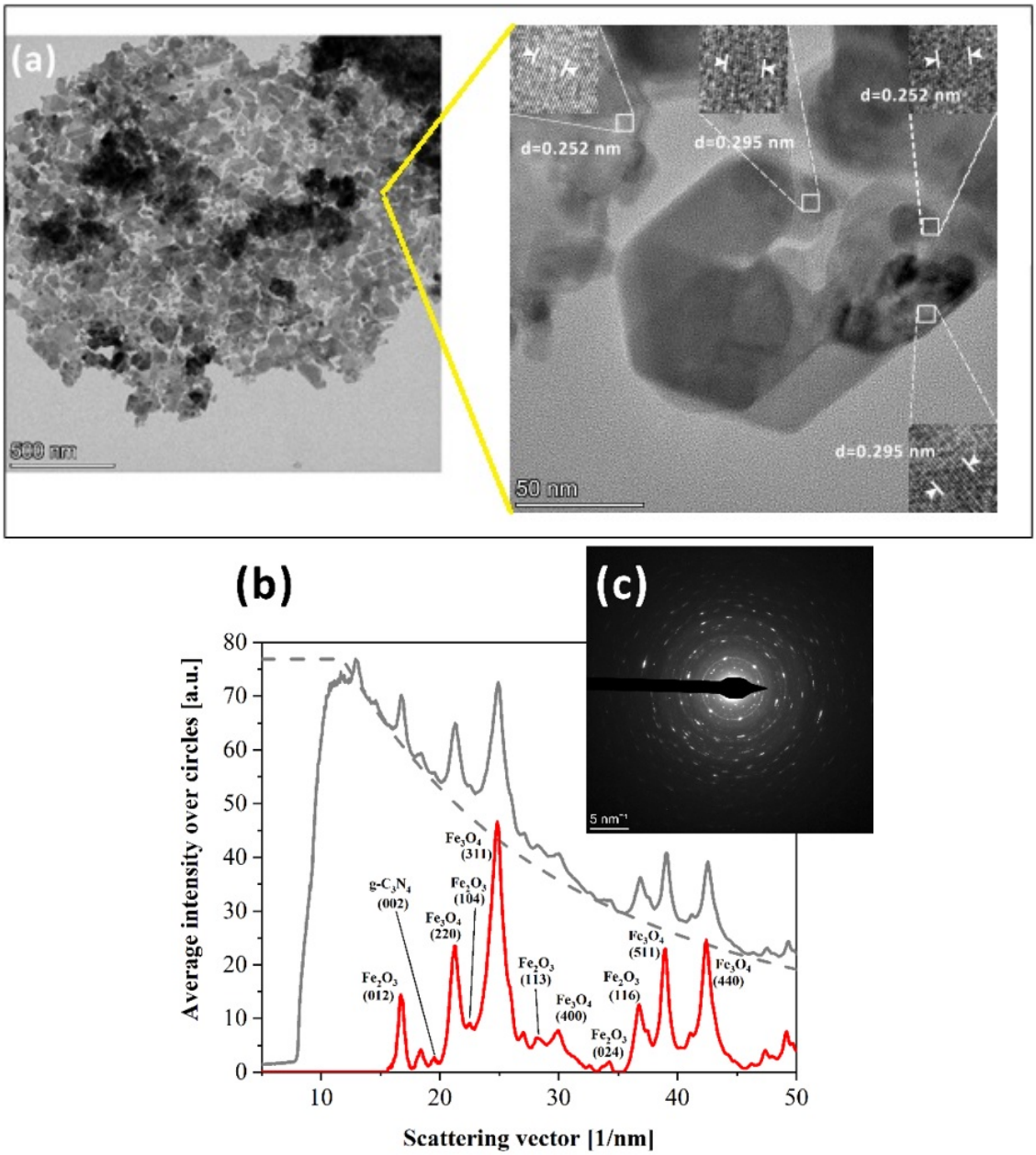

Figure 9. (FeOx/g-C_3N_4)*in* TEM and HRTEM analysis (**a**). Bright field TEM image of a crystalline petal whose SAED diffraction pattern is given in (**c**). The intensity profile obtained from (**c**) is shown in (**b**): gray lines indicate gross intensity (solid line) and the subtracted background (dashed line), and the red line is the resulting net intensity.

3.3. XPS Analysis

XPS was used to analyse the chemical bonding and composition of all the prepared materials. Figure 10 presents the full survey scan of the FeOx iron urchins, (FeOx/g-C_3N_4)*in*, and (FeOx/g-C_3N_4)*ex* composites that are compared to the FeOx as a support material only. The XPS survey spectra reveals presence of Fe, O, N, and C.

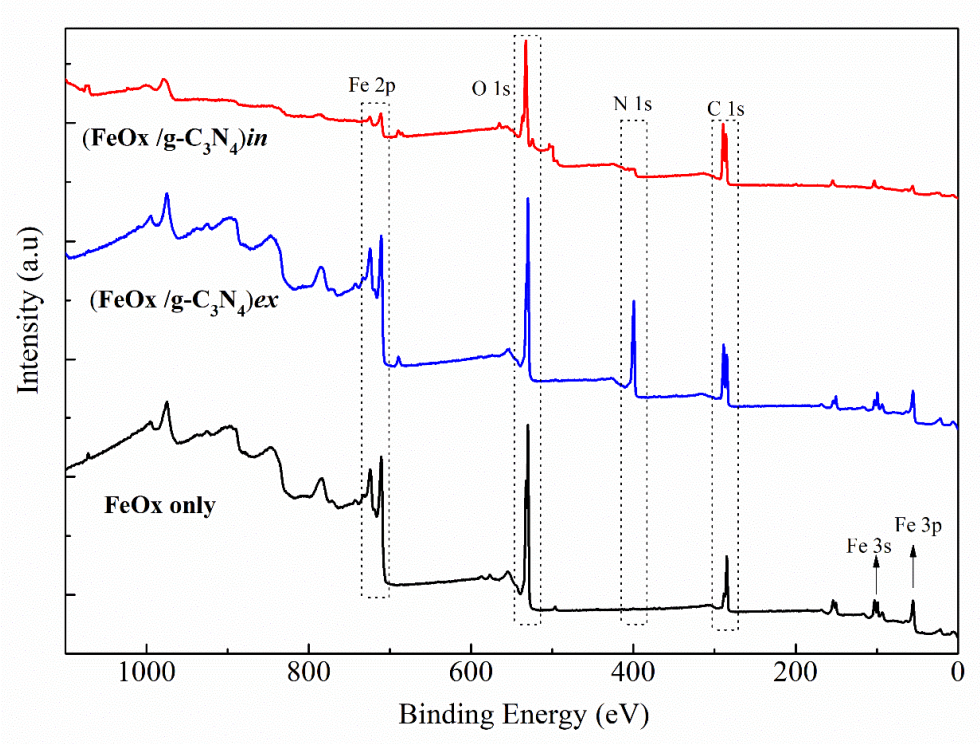

Figure 10. XPS survey scan for all elements in the FeOx urchin and its composites with g-C_3N_4.

Figure 11 shows Fe $2p_{3/2}$ core level spectra of FeOx and its composites, the Fe 2p survey can be found in the Supplementary Materials (Figure S12a). The Fe $2p_{3/2}$ core level main peak position (without curve fitting) is located at around 711 eV binding energy (BE) with spin-orbit splitting and a satellite at 719 eV. The peak at 711 eV was further deconvoluted into three peaks, namely 709.8 eV, 710.8 eV, and 712 eV, which correspond to +3 oxidation state of alpha hematite [62–64]. This clearly indicates the presence of dominating alpha Fe_2O_3 phase (hematite) with the +3 oxidation state on the surface of FeOx and (FeOx/g-C_3N_4)*ex* samples. For the XPS spectra of (FeOx/g-C_3N_4)*in*, the main BE positions at 711.5 eV with spin-orbit splitting indicate the presence of a Fe_3O_4 phase. Therefore, the presence of both hematite and Fe_3O_4 cannot be excluded in the samples, thus further supporting our previously reported (Figure 4) XRD results. In Figure 12a, the C1s spectrum of the composite materials contains two peaks at 285 eV and 288.9 eV for (FeOx/g-C_3N_4)*in*, which arise from C–N and sp^2-hybridized C in N=C–N. However, for (FeOx/g-C_3N_4)*ex*, the peaks originate at 285.1 eV and 289.3 eV [65,66]. Thus, the C 1s core level spectra of both composite films, i.e., (FeOx/g-C_3N_4)*ex* and (FeOx/g-C_3N_4)*in*, clearly show the presence of the C–N bonding structure coming from g-C_3N_4 with specific contributions as shown in adjacent peaks resulting from the fitted components. A slight modification of peak positions related to g-C_3N_4 was observed in case of the (FeOx/g-C_3N_4)*in* composite film, which could be attributed to interface effects with FeOx [65–70].

The N 1s spectrum (Figure 12b) related to (FeOx/g-C_3N_4)*in* is deconvoluted into three different peaks at 399.8, 401.5, and 402.1 eV, which are attributed, respectively, to sp^2-hybridized N in C=N–C, sp^3-hybridized N in N–C_3, and C-N-H from amino groups and π excitations in heterocycles. The N 1s core level spectra also clearly indicate the respective bonding contributions (reported with fitted components) originating from the g-C_3N_4 chemical structure. It is also interesting to see that the fitted components with respective chemical structures show modifications in the intensity as well. This is not fully understood yet but probably results from minor changes in the atomic lattice arrangement. Also, the O 1s spectra reported in the Figure S12b, identifies the presence of Fe-O chemical bonding as in Fe oxides with two peaks at 530 eV and 532.6 eV arising from the lattice oxygen in FeOx and the related hydroxide-oxyhydroxide system [71,72]. The small peak

around 532 eV is associated with the presence of adsorbed water on the surface of the samples [73].

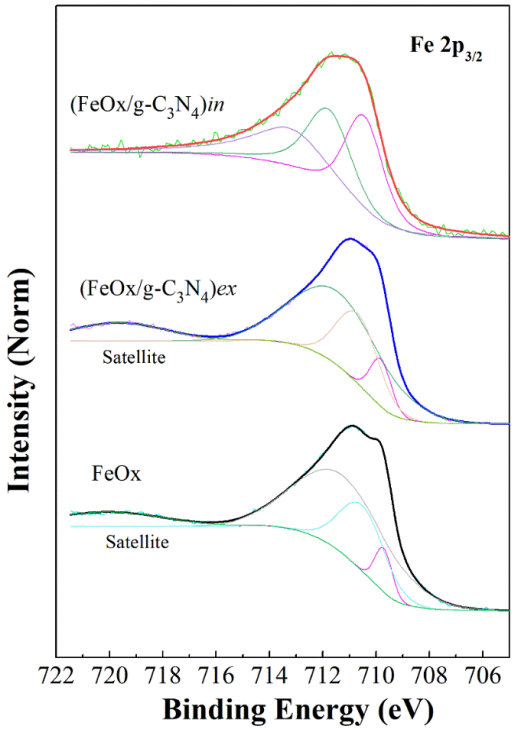

Figure 11. XPS spectra of the Fe 2p3/2 core level and deconvolution peaks of the iron urchin and its composites with g-C3N4. All the spectra were normalized to the maximum of the peak and curve fitting was achieved using Shirley background and Voigt profiles.

Moreover, looking at the lower bandgap (inset in Figure 5) of the (FeOx/g-C3N4)*in* thin film with respect to (FeOx/g-C3N4)*ex*, we can suggest that the detected minor differences (1.87 vs. 1.95 eV) could also be related to slight changes in atomic lattice arrangement in the in situ-produced g-C3N4 and FeOx likely promoting charge carrier separation and mobility.

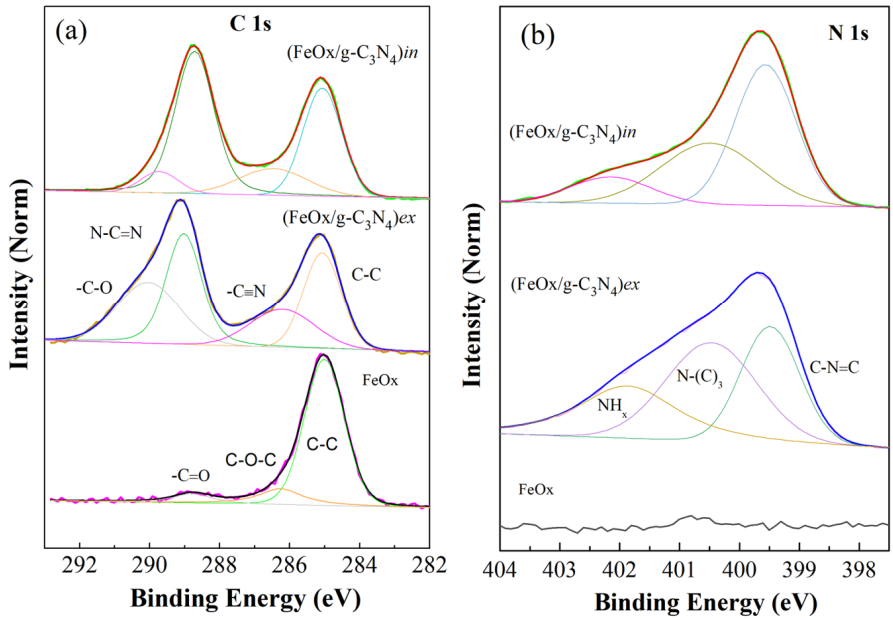

Figure 12. XPS spectra of (**a**) C 1s and (**b**) N 1s core levels and the corresponding deconvolution peaks of the iron urchin and its composites with g-C_3N_4. All the spectra were normalized to the maximum of the peak and curve fitting was achieved using Shirley background and Voigt profiles.

3.4. Photocatalytic Activity

The photocatalytic activity of the prepared materials was evaluated at the proof-of-concept level in CIP degradation. First the g-C_3N_4 dispersed powder and coating samples were tested. The adsorption of powders and the poor photocatalytic degradation of CIP in films and powders was observed (Figure S13). Also, the (FeOx/g-C_3N_4)*ex* thin films show only 5% CIP disappearance after 180 min irradiation (Figure S14). The observed inferior CIP removal of (FeOx/g-C_3N_4)*ex* was due to the weak g-C_3N_4 adhesion with consequent partial detachment during the experiment, as pointed out by SEM. Therefore, we have not performed further in-depth analysis of these samples.

The photocatalytic activity of the (FeOx/g-C_3N_4)*in* thin films were compared in the photocatalytic removal of CIP through visible irradiation. Results are reported in Figure 13, and the corresponding UV–Vis spectra obtained are reported in Supplementary Figure S16. Low adsorption (less than 5%) is observed in the dark during the equilibrium period. Upon visible illumination, the system (FeOx/g-C_3N_4)*in* shows a better performance and leads to a 14% of CIP disappearance after 180 min of irradiation with a kinetic constant of 8.28×10^{-4} min^{-1}. The results obtained via (FeOx/g-C_3N_4)*in* are of relevance if one considers the control experiments reported in Figure S15. It is observed that both thermolysis at 50 °C and visible irradiation in the absence of a photocatalyst (photolysis) do not cause any decrease in CIP concentration. This demonstrates that the presence of the composite (FeOx/g-C_3N_4)*in* is mandatory for achieving CIP degradation and that degradation is not a consequence of the temperature increase from the heat developed by the radiation system or photolysis.

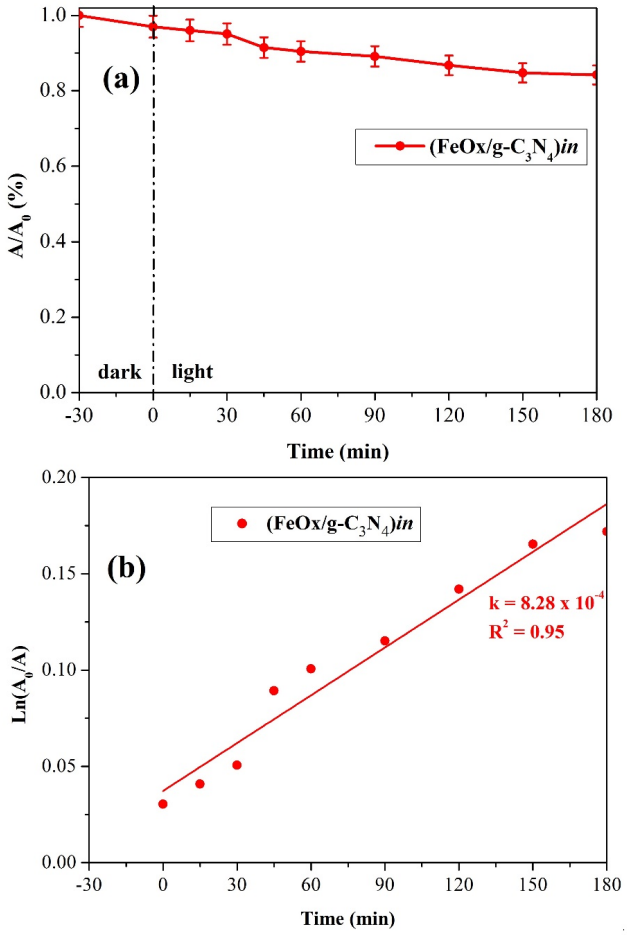

Figure 13. (**a**) removal yields and (**b**) corresponding reaction kinetics of the CIP upon irradiation of (FeOx/g-C_3N_4)*in* immersed in aqueous solutions containing CIP (C_0 = 10 ppm).

Given the results obtained from (FeOx/g-C_3N_4)*in*, the photo-Fenton reaction was tested with the addition of H_2O_2. Results are reported in Figure 14, where experiments performed with FeOx alone and in the presence of H_2O_2 5 × 10^{-4} M are reported for comparison. The irradiation of FeOx alone (black) caused a disappearance of CIP of about 15%. When H_2O_2 (5 × 10^{-4} M) is present, the material showed a higher CIP disappearance in the dark (17%), possibly due to an initial Fenton reaction, and upon irradiation a disappearance of 35% of CIP is observed with moderate improvements of the degradation after the initial 60 min of illumination on both photo-Fenton cases (FeOx + H_2O_2 and (FeOx/g-C_3N_4)*in* + H_2O_2). This moderate enhancement of degradation is attributed to slight temperature changes and is consistent with the literature [74]. The calculated kinetic constant is k = 1.6 × 10^{-3} min^{-1}. A comparison of the results of FeOx (Figure 14) with (FeOx/g-C_3N_4)*in* (Figure 13) shows that their photocatalytic activities are very similar. However, the addition of H_2O_2 (5 × 10^{-4} M) to the aqueous solution of CIP in which (FeOx/g-C_3N_4)*in* is present had a booster effect: in fact, 60% of CIP disappearance is achieved after irradiation, a value significantly higher than that observed with FeOx and (5 × 10^{-4} M) H_2O_2 alone (6%).

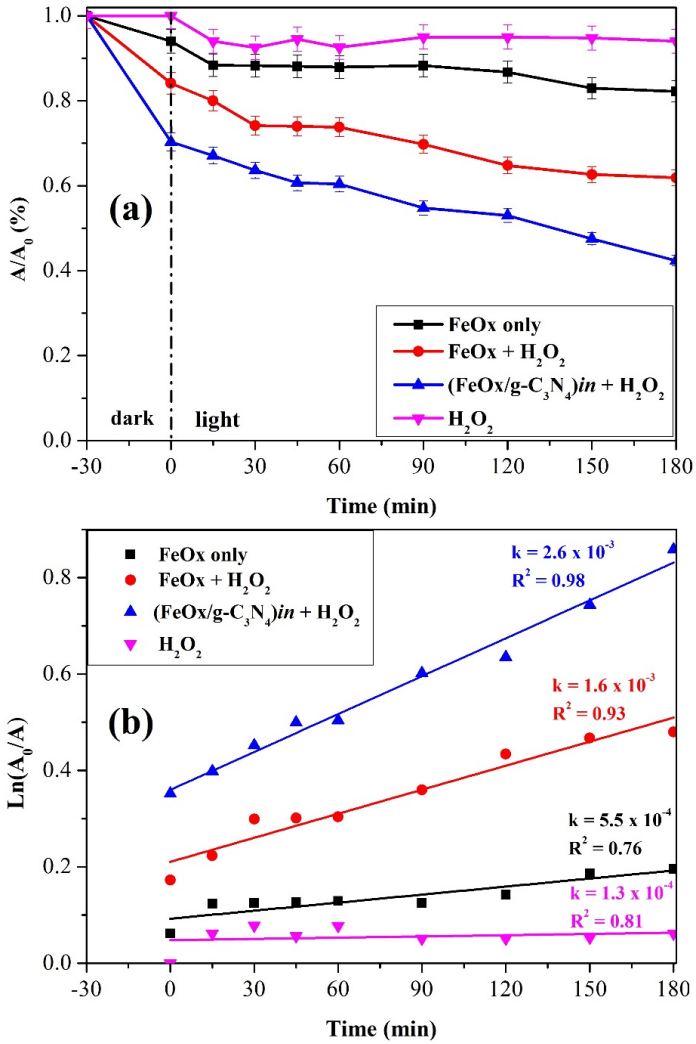

Figure 14. Removal yields (**a**) and reaction kinetics (**b**) of the CIP disappearance upon the irradiation of FeOx (black), FeOx + H_2O_2 (5 × 10^{-4} M) (red), and FeOx/g-C_3N_4 composites + H_2O_2 (5 × 10^{-4} M) (blue). The starting concentration of CIP is 10 ppm.

Therefore, the photo-Fenton process further enhances the degradation efficiency of the (FeOx/g-C_3N_4)*in* composite material compared with the two parts alone. In addition, good adhesion over the glass slides was observed both during photocatalysis and the photo-Fenton reaction.

An overview of the results obtained during the photocatalytic and photo-Fenton experiments are provided in Table 1.

Table 1. Summary of the testing conditions and results for the photocatalysts.

Experimental Condition	Catalyst Form	CIP Adsorption	CIP Removal Yield	Kinetic Constant (k, min^{-1})
H_2O_2 (5×10^{-4} M)	No catalyst	0%	6%	1.3×10^{-4}
(FeOx/g-C_3N_4)*in*		5%	13%	8.28×10^{-4}
FeOx		5%	15%	5.5×10^{-4}
FeOx + H_2O_2 (5×10^{-4} M)		17%	35%	1.6×10^{-3}
(FeOx/g-C_3N_4)*in* + H_2O_2 (5×10^{-4} M)		30%	60%	2.6×10^{-3}

It has been observed that the (FeOx/g-C_3N_4)*in* composite material exhibits very important photoactivity during CIP removal under photo-Fenton conditions, showing an increase of one order of magnitude of the relative kinetic constant. This activity is higher than that of each counterpart alone. This picture is compatible with the arising of a heterojunction effect, such as a complete (where the solid–liquid interfaces of both materials are redox active) or partial (where only one, i.e., the FeOx conduction band is redox active) Z-scheme in the composite. Another possible explanation for the enhanced performance in the composite is that g-C_3N_4 is simply acting as an electron acceptor, thus temporarily trapping electrons from the FeOx conduction band and inhibiting charge recombination [75]. We consider this last scenario unlikely, as the bandgap of g-C_3N_4 is also compatible with visible absorption.

A likely photocatalysis mechanism for the (FeOx/g-C_3N_4)*in* composite, presented in Figure 15, can be hypothesized based on our data and the current literature. It is known that the degradation of CIP in the presence of iron oxides and g-C_3N_4 occurs mainly through the formation of active species, i.e., superoxide radicals (O_2^-), hydroxyl radical (·OH), and holes (h+) [30,48,76–80]. In the case of (FeOx/g-C_3N_4)*in*, the degradation of CIP is then expected to proceed via two different pathways depending on whether H_2O_2 is present or not. Without H_2O_2 (Figure 15a), the CIP degradation probably proceeds through the formation of a Z-scheme between FeOx and g-C_3N_4 where primarily the (O_2^-) and (·OH) active species are produced. Note that in this case, ·OH can only be produced through the reaction between h+ and water [78–82] and that the superoxide radicals are not very efficient in reacting with CIP [76,83]. When H_2O_2 is added, ·OH can also be produced through the reactions between CB electrons and H_2O_2 and between superoxide and H_2O_2, (Figure 15b) [76,83–87], resulting in a greater availability of highly active ·OH, which would explain the higher activity in the photo-Fenton mode. A detailed investigation of the composite materials working mechanism via transient UV–visible spectroscopy and using selective radical inhibitors will be undertaken in future investigations to confirm this mechanism hypothesis. Nevertheless, we consider the results reported here as a proof-of-concept that the in situ approach is a viable route for achieving heterojunction effects on thin-film photocatalysts for application in pollutant degradation. This is proven by data in Table 2 where a comparison is reported between the best results we obtained with the (FeOx/g-C_3N_4)*in* +H_2O_2 (5×10^{-4} M) samples and literature data (90-97) for the removal of ciprofloxacin in water and additional information can also be found from literature [88–91].

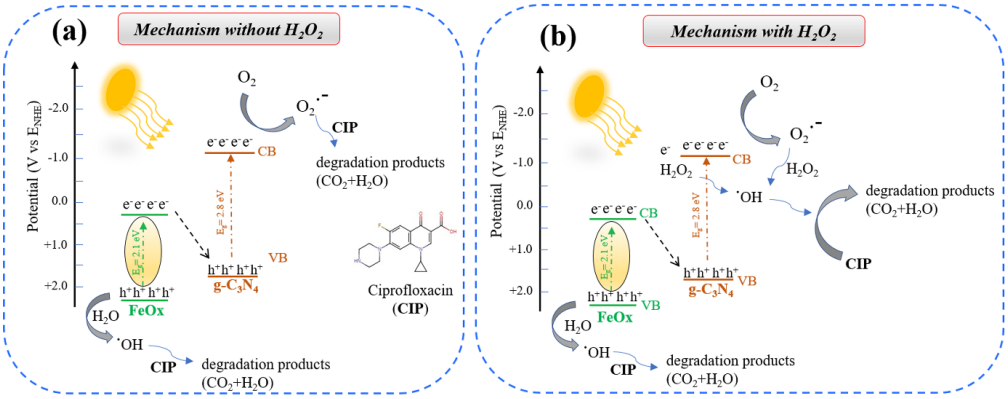

Figure 15. Schematic showing the (FeOx/g-C_3N_4)*in* photocatalyst degradation mechanism (**a**) without H_2O_2 and (**b**) with H_2O_2.

Table 2. Comparison for CIP removal with photocatalysts.

Ref	Catalyst	CIP Concentration (ppm)	Tested Volume (mL)	Experimental Time (min)	Illumination Source	Removal Yield
[92]	N,S-CQDs/Bi_2MoO_6@TiO_2	20	15	270	Visible light ca. 200 mW/cm²	90%
[93]	FTO/$BaTiO_3$/SnO_2	5	75	180	100 W Xe lamp + Ultrasound 24 KHz	60%
[94]	Bi_2MoO_6@Bi_2MoO_{6-x}	20	100	150	6.2 W LEDs between 400 and 700 nm	95%
[95]	TiO_2 MOCVD	20	100	480	UV LED 365 nm	100%
[96]	(nc-TiO_2) from Degussa P25	10	100	600	UV lamp 276 nm	100%
[97]	TiO_2 films grown electrochemically	40	190	180	UV lamp (100–280 nm)	70%
[98]	Ag_2MoO_4	20	100	40	UV lamp (200–400 nm)	90%
[99]	CeO_2/CuO/ZnO/Zn	10	100	120	Mercury lamp 120 W—UV light	70%
This work	(FeOx/g-C_3N_4)*in* + H_2O_2 (5×10^{-4} M)	10	50	180	Visible Halogen lamps, 225W	60%

4. Conclusions

The development of composites produced by combining iron oxide urchins (FeOx) with g-C_3N_4 following two different procedures (FeOx/g-C_3N_4)*in* and (FeOx/g-C_3N_4)*ex* was reported along with its application in the photocatalytic degradation of ciprofloxacin pharmaceuticals.

The PLD procedure to obtain annealed hematite iron urchins followed by the drop-casting of the melamine precursor to thermally condense the g-C_3N_4 (FeOx/g-C_3N_4)*in* composite thin film evolved into to a petal-like morphology with a high surface area featuring good absorption in the visible range (<600 nm). This composite material exhibits an improved photocatalytic performance when compared to the single components, with the optimal condition for ciprofloxacin degradation (from 20 to nearly 60%) observed under the photo-Fenton condition. These results are compatible with a heterojunction effect in the composite, likely of the Z-scheme type. The advantages with (FeOx/g-C_3N_4)*in* rely on the mechanical stability of the coating on the glass surface, which allows us to overcome the problems related to the use of nanoparticles in suspension. The research presented in this paper will be further developed as we consider the reported results as a significant

starting point for obtaining a Z-scheme strategy specifically for thin-films. Indeed, further activities aimed at elucidating the working mechanism of these composites under light are ongoing.

Supplementary Materials: The following supporting information can be downloaded at: https://www.mdpi.com/article/10.3390/app131910591/s1, Section S1: Different aspects regarding ex situ and in situ materials synthesis methods, Section S2: light source for photocatalysis experiments, Section S3: characterisation of g-C3N4 bulk and Section S4: FeOx composite films, Section S6: Raman peak assignments, Section S5: supporting information for photocatalytic tests, and Section S7: UV–Vis spectra from the photocatalysis experiments. Figure S1: Measured and normalized spectrum of visible light lamps (75 W each) employed in this work (Osram HALOPAR 30, 75 W, 30°aperture angle, luminous flux of 350 lumens); Figure S2: Absorption spectrum of melamine used as precursor to g-C3N4 synthesis; Figure S3: SEM image of g-C3N4 powder synthesized at 550 °C 4h and its corresponding EDXS spectra; Figure S4: FTIR spectra of the melamine and g-C3N4 synthesized at 550 °C 4 h; Figure S5: Raman spectra of melamine and g-C3N4 synthesized at 550 °C 4h; Figure S6: GIXRD pattern of the synthesized g-C3N4 powder at 550 °C; Figure S7: UV-Vis absorption spectra and Tauc plot of the g-C3N4 synthesized at 550 °C 4h; Figure S8: EDXS spectrum of the surface of the FeOx urchin like structures used as support in the composite with g-C3N4; Figure S9: EDXS spectra from 4 different regions of the (FeOx/g-C3N4)in composite thin films; Figure S10: EDXS spectra from two different regions of the (FeOx/g-C3N4)*ex* composite thin films; Fig. S11 (FeOx/g-C3N4)*in* TEM image and corresponding larger area SAED pattern; Figure S12 XPS spectra of (a) Fe 2p (top left) and specifically Fe 2p3/2 (top right) and (b) O1s core levels without curve fitting of the iron urchin and its composites with g-C3N4; Figure S13: Removal yields of the CIP disappearance upon irradiation of g-C3N4 4h in powder (black) and in the film (blue) in aqueous solutions containing CIP (C0 = 10 ppm); Figure S14: Removal yields of the CIP disappearance upon irradiation of (FeOx/g-C3N4)*ex* thin films immersed in aqueous solutions containing CIP (C0 = 10 ppm); Figure S15: Control experiments: aerated aqueous solution of CIP (10 ppm) maintained at 50°C in the dark (red) or visible irradiated (blue) in the absence of any photocatalyst; Table S1: modes of every peak identified in the Raman measurements. The peaks identifications are based on the literature [100–103]; Figure S16: UV-Vis spectra from obtained from the photocatalysis and photo-Fenton experiments.

Author Contributions: Conceptualisation: M.F., O.P.B. and M.O.; sample preparation and analysis: M.F., O.P.B., R.E., A.M. (Alessandra Molinari), P.R. and C.M.; original draft preparation: M.F. and O.P.B.; writing—Review and editing: M.O., A.M. (Antonio Miotello), A.M. (Alessandra Molinari), R.E. and C.M.; supervision: M.O. and A.M. (Antonio Miotello); funding acquisition: A.M. (Antonio Miotello) and M.O. All authors have read and agreed to the published version of the manuscript.

Funding: This work was supported by the ERICSOL project, funded by the University of Trento, and by the FarSol project, funded by the Caritro Foundation (Research & Development 2020 Grant). We also acknowledge project "Produrre Idrogeno in Trentino—H2@TN" (PAT-Trento). Chiara Maurizio and Paola Ragonese acknowledge project FUN-FACE (SID_2019) of the Physics and Astronomy Department of the University of Padova (Italy).

Institutional Review Board Statement: Not applicable.

Informed Consent Statement: Not applicable.

Data Availability Statement: Raw data or datasets not included here are available from the authors upon request.

Acknowledgments: We thank Nicola Bazzanella for SEM/TEM measurements and Mario Rossi for FT-IR support.

Conflicts of Interest: The authors declare no conflict of interest.

References

1. Xu, Q.; Zhang, L.; Yu, J.; Wageh, S.; Al-Ghamdi, A.A.; Jaroniec, M. Direct Z-scheme photocatalysts: Principles, synthesis, and applications. *Mater. Today* **2018**, *21*, 1042–1063. https://doi.org/10.1016/j.mattod.2018.04.008.
2. Ghorai, K.; Panda, A.; Hossain, A.; Bhattacharjee, M.; Chakraborty, M.; Bhattacharya, S.K.; Show, B.; Sarkar, A.; Bera, P.; Kim, H.; et al. $LaNiO_3$/g-C_3N_4 nanocomposite: An efficient Z-scheme photocatalyst for wastewater treatment using direct sunlight. *J. Rare Earths* **2022**, *40*, 725–736. https://doi.org/10.1016/j.jre.2021.04.013.

3. Xu, C.; Zhou, Q.; Huang, W.-Y.; Yang, K.; Zhang, Y.-C.; Liang, T.-X.; Liu, Z.-Q. Constructing Z-scheme β-Bi_2O_3/ZrO_2 heterojunctions with 3D mesoporous SiO_2 nanospheres for efficient antibiotic remediation via synergistic adsorption and photocatalysis. *Rare Met.* **2022**, *41*, 2094–2107. https://doi.org/10.1007/s12598-021-01897-9.
4. Guo, X.; Duan, J.; Li, C.; Zhang, Z.; Wang, W. Highly efficient Z-scheme g-C_3N_4/ZnO photocatalysts constructed by co-melting-recrystallizing mixed precursors for wastewater treatment. *J. Mater. Sci.* **2020**, *55*, 2018–2031. https://doi.org/10.1007/s10853-019-04097-0.
5. Yuan, Y.; Zhang, L.; Xing, J.; Utama, M.I.B.; Lu, X.; Du, K.; Li, Y.; Hu, X.; Wang, S.; Genç, A.; et al. High-yield synthesis and optical properties of g-C_3N_4. *Nanoscale* **2015**, *7*, 12343–12350. https://doi.org/10.1039/c5nr02905h.
6. Chen, Z.; Zhang, S.; Liu, Y.; Alharbi, N.S.; Rabah, S.O.; Wang, S.; Wang, X. Synthesis and fabrication of g-C_3N_4-based materials and their application in elimination of pollutants. *Sci. Total Environ.* **2020**, *731*, 139054. https://doi.org/10.1016/j.scitotenv.2020.139054.
7. Schwarzer, A.; Saplinova, T.; Kroke, E. Tri-s-triazines (s-heptazines)-From a "mystery molecule" to industrially relevant carbon nitride materials. *Coord. Chem. Rev.* **2013**, *257*, 2032–2062. https://doi.org/10.1016/j.ccr.2012.12.006.
8. Song, G.; Chu, Z.; Jin, W.; Sun, H. Enhanced performance of g-C_3N_4/TiO_2 photocatalysts for degradation of organic pollutants under visible light. *Chin. J. Chem. Eng.* **2015**, *23*, 1326–1334. https://doi.org/10.1016/j.cjche.2015.05.003.
9. Jo, W.K.; Natarajan, T.S. Influence of TiO_2 morphology on the photocatalytic efficiency of direct Z-scheme g-C_3N_4/TiO_2 photocatalysts for isoniazid degradation. *Chem. Eng. J.* **2015**, *281*, 549–565. https://doi.org/10.1016/j.cej.2015.06.120.
10. Hu, K.; Li, R.; Ye, C.; Wang, A.; Wei, W.; Hu, D.; Qiu, R.; Yan, K. Facile synthesis of Z-scheme composite of TiO_2 nanorod/g-C_3N_4 nanosheet efficient for photocatalytic degradation of ciprofloxacin. *J. Clean. Prod.* **2020**, *253*, 120055. https://doi.org/10.1016/j.jclepro.2020.120055.
11. Lettieri, S.; Pavone, M.; Fioravanti, A.; Amato, L.S.; Maddalena, P. Charge carrier processes and optical properties in TiO_2 and TiO_2-based heterojunction photocatalysts: A review. *Materials* **2021**, *14*, 1645. https://doi.org/10.3390/ma14071645.
12. Zhou, D.; Chen, Z.; Yang, Q.; Shen, C.; Tang, G.; Zhao, S.; Zhang, J.; Chen, D.; Wei, Q.; Dong, X. Facile Construction of g-C_3N_4 Nanosheets/TiO_2 Nanotube Arrays as Z-Scheme Photocatalyst with Enhanced Visible-Light Performance. *ChemCatChem* **2016**, *8*, 3064–3073. https://doi.org/10.1002/cctc.201600828.
13. Li, X.; Wang, B.; Yin, W.; Di, J.; Xia, J.; Zhu, W.; Li, H. Cu^{2+} modified g-C_3N_4 photocatalysts for visible light photocatalytic properties. *Acta Phys. Chim. Sin.* **2020**, *36*, 1902001. https://doi.org/10.3866/PKU.WHXB201902001.
14. Zhu, H.; Yang, B.; Yang, J.; Yuan, Y.; Zhang, J. Persulfate-enhanced degradation of ciprofloxacin with SiC/g-C_3N_4 photocatalyst under visible light irradiation. *Chemosphere* **2021**, *276*, 130217. https://doi.org/10.1016/j.chemosphere.2021.130217.
15. Li, H.; Jing, Y.; Ma, X.; Liu, T.; Yang, L.; Liu, B.; Yin, S.; Wei, Y.; Wang, Y. Construction of a well-dispersed Ag/graphene-like g-C_3N_4 photocatalyst and enhanced visible light photocatalytic activity. *RSC Adv.* **2017**, *7*, 8688–8693. https://doi.org/10.1039/C6RA26498K.
16. Zhu, Z.; Lu, Z.; Wang, D.; Tang, X.; Yan, Y.; Shi, W.; Wang, Y.; Gao, N.; Yao, X.; Dong, H. Construction of high-dispersed Ag/Fe_3O_4/g-C_3N_4 photocatalyst by selective photo-deposition and improved photocatalytic activity. *Appl. Catal. B Environ.* **2016**, *182*, 115–122. https://doi.org/10.1016/j.apcatb.2015.09.029.
17. Wang, F.; Zhu, Z.; Guo, J. 2D-2D ZnO/N doped g-C_3N_4 composite photocatalyst for antibiotics degradation under visible light. *RSC Adv.* **2021**, *11*, 35663–35672. https://doi.org/10.1039/d1ra06607b.
18. He, F.; Chen, G.; Yu, Y.; Hao, S.; Zhou, Y.; Zheng, Y. Facile approach to synthesize g-PAN/g-C_3N_4 composites with enhanced photocatalytic H_2 evolution activity. *ACS Appl. Mater. Interfaces* **2014**, *6*, 7171–7179. https://doi.org/10.1021/am500198y.
19. Munusamy, T.D.; Yee, C.S.; Khan, M.M.R. Construction of hybrid g-C_3N_4/CdO nanocomposite with improved photodegradation activity of RhB dye under visible light irradiation. *Adv. Powder Technol.* **2020**, *31*, 2921–2931. https://doi.org/10.1016/j.apt.2020.05.017.
20. Yoon, M.; Oh, Y.; Hong, S.; Lee, J.S.; Boppella, R.; Kim, S.H.; Marques Mota, F.; Kim, S.O.; Kim, D.H. Synergistically enhanced photocatalytic activity of graphitic carbon nitride and WO_3 nanohybrids mediated by photo-Fenton reaction and H_2O_2. *Appl. Catal. B Environ.* **2017**, *206*, 263–270. https://doi.org/10.1016/j.apcatb.2017.01.038.
21. Safaei, J.; Mohamed, N.A.; Noh, M.F.M.; Soh, M.F.; Riza, M.A.; Mustakim, N.S.M.; Ludin, N.A.; Ibrahim, M.A.; Isahak, W.N.R.W.; Teridi, M.A.M. Facile fabrication of graphitic carbon nitride, (g-C_3N_4) thin film. *J. Alloys Compd.* **2018**, *769*, 130–135. https://doi.org/10.1016/j.jallcom.2018.07.337.
22. Mohamed, N.A.; Safaei, J.; Ismail, A.F.; Jailani, M.F.A.M.; Khalid, M.N.; Noh, M.F.M.; Aadenan, A.; Nasir, S.N.S.; Sagu, J.S.; Teridi, M.A.M. The influences of post-annealing temperatures on fabrication graphitic carbon nitride, (g-C_3N_4) thin film. *Appl. Surf. Sci.* **2019**, *489*, 92–100. https://doi.org/10.1016/j.apsusc.2019.05.312.
23. Zhang, Y.; Zhao, S.-M.; Su, Q.-W.; Xu, J.-L. Visible light response ZnO–C_3N_4 thin film photocatalyst. *Rare Met.* **2021**, *40*, 96–104. https://doi.org/10.1007/s12598-019-01297-0.
24. Zhao, W.; Yang, X.; Liu, C.; Qian, X.; Wen, Y.; Yang, Q.; Sun, T.; Chang, W.; Liu, X.; Chen, Z. Facile Construction of All-Solid-State Z-Scheme g-C_3N_4/TiO_2 Thin Film for the Efficient Visible-Light Degradation of Organic Pollutant. *Nanomaterials* **2020**, *10*, 600.
25. Nandy, S.; Savant, S.A.; Haussener, S. Prospects and challenges in designing photocatalytic particle suspension reactors for solar fuel processing. *Chem. Sci.* **2021**, *12*, 9866–9884. https://doi.org/10.1039/D1SC01504D.
26. Fendrich, M.; Popat, Y.; Orlandi, M.; Quaranta, A.; Miotello, A. Pulsed laser deposition of nanostructured tungsten oxide films: A catalyst for water remediation with concentrated sunlight. *Mater. Sci. Semicond. Process.* **2020**, *119*, 105237. https://doi.org/10.1016/j.mssp.2020.105237.

27. El Golli, A.; Fendrich, M.; Bazzanella, N.; Dridi, C.; Miotello, A.; Orlandi, M. Wastewater remediation with ZnO photocatalysts: Green synthesis and solar concentration as an economically and environmentally viable route to application. *J. Environ. Manag.* **2021**, *286*, 112226. https://doi.org/10.1016/j.jenvman.2021.112226.
28. Sun, Z.; Zhang, X.; Zhu, R.; Dong, X.; Xu, J.; Wang, B. Facile synthesis of visible light-induced g-C_3N_4/rectorite composite for efficient photodegradation of ciprofloxacin. *Materials* **2018**, *11*, 2452. https://doi.org/10.3390/ma11122452.
29. Song, Y.; Tian, J.; Gao, S.; Shao, P.; Qi, J.; Cui, F. Photodegradation of sulfonamides by g-C_3N_4 under visible light irradiation: Effectiveness, mechanism and pathways. *Appl. Catal. B Environ.* **2017**, *210*, 88–96. https://doi.org/10.1016/j.apcatb.2017.03.059.
30. Suyana, P.; Ganguly, P.; Nair, B.N.; Pillai, S.C.; Hareesh, U.S. Structural and compositional tuning in g-C_3N_4 based systems for photocatalytic antibiotic degradation. *Chem. Eng. J. Adv.* **2021**, *8*, 100148. https://doi.org/10.1016/j.ceja.2021.100148.
31. Nguyen, T.B.; Huang, C.P.; Doong, R.-A.; Chen, C.W.; Dong, C. Di Visible-light photodegradation of sulfamethoxazole (SMX) over Ag-P-codoped g-C_3N_4 (Ag-P@UCN) photocatalyst in water. *Chem. Eng. J.* **2020**, *384*, 123383. https://doi.org/10.1016/j.cej.2019.123383.
32. Li, G.; Nie, X.; Gao, Y.; An, T. Can environmental pharmaceuticals be photocatalytically degraded and completely mineralized in water using g-C_3N_4/TiO_2 under visible light irradiation?-Implications of persistent toxic intermediates. *Appl. Catal. B Environ.* **2016**, *180*, 726–732. https://doi.org/10.1016/j.apcatb.2015.07.014.
33. Mohamed, R.M. Synthesis and characterization of AgCl@graphitic carbon nitride hybrid materials for the photocatalytic degradation of atrazine. *Ceram. Int.* **2015**, *41*, 1197–1204. https://doi.org/10.1016/j.ceramint.2014.09.048.
34. Geng, Y.; Chen, D.; Li, N.; Xu, Q.; Li, H.; He, J.; Lu, J. Z-Scheme 2D/2D α-Fe_2O_3/g-C_3N_4 heterojunction for photocatalytic oxidation of nitric oxide. *Appl. Catal. B Environ.* **2021**, *280*, 119409. https://doi.org/10.1016/j.apcatb.2020.119409.
35. Alduhaish, O.; Ubaidullah, M.; Al-Enizi, A.M.; Alhokbany, N.; Alshehri, S.M.; Ahmed, J. Facile Synthesis of Mesoporous α-Fe_2O_3@g-C_3N_4-NCs for Efficient Bifunctional Electro-catalytic Activity (OER/ORR). *Sci. Rep.* **2019**, *9*, 14139. https://doi.org/10.1038/s41598-019-50780-2.
36. Wang, Z.; Fan, Y.; Wu, R.; Huo, Y.; Wu, H.; Wang, F.; Xu, X. Novel magnetic g-C_3N_4/α-Fe_2O_3/Fe_3O_4 composite for the very effective visible-light-fenton degradation of Orange II. *RSC Adv.* **2018**, *8*, 5180–5188. https://doi.org/10.1039/c7ra13291c.
37. Vesborg, P.C.K.; Jaramillo, T.F. Addressing the terawatt challenge: Scalability in the supply of chemical elements for renewable energy. *RSC Adv.* **2012**, *2*, 7933–7947. https://doi.org/10.1039/C2RA20839C.
38. aus der Beek, T.; Weber, F.-A.; Bergmann, A.; Hickmann, S.; Ebert, I.; Hein, A.; Küster, A. Pharmaceuticals in the environment—Global occurrences and perspectives. *Environ. Toxicol. Chem.* **2016**, *35*, 823–835. https://doi.org/10.1002/etc.3339.
39. Ribeiro, A.R.; Nunes, O.C.; Pereira, M.F.R.; Silva, A.M.T. An overview on the advanced oxidation processes applied for the treatment of water pollutants defined in the recently launched Directive 2013/39/EU. *Environ. Int.* **2015**, *75*, 33–51. https://doi.org/10.1016/j.envint.2014.10.027.
40. Edla, R.; Tonezzer, A.; Orlandi, M.; Patel, N.; Fernandes, R.; Bazzanella, N.; Date, K.; Kothari, D.C.; Miotello, A. 3D hierarchical nanostructures of iron oxides coatings prepared by pulsed laser deposition for photocatalytic water purification. *Appl. Catal. B Environ.* **2017**, *219*, 401–411. https://doi.org/10.1016/j.apcatb.2017.07.063.
41. Popat, Y.; Orlandi, M.; Patel, N.; Edla, R.; Bazzanella, N.; Gupta, S.; Yadav, M.; Pillai, S.; Patel, M.K.; Miotello, A. Pulsed laser deposition of $CoFe_2O_4$/CoO hierarchical-type nanostructured heterojuction forming a Z-scheme for efficient spatial separation of photoinduced electron-hole pairs and highly active surface area. *Appl. Surf. Sci.* **2019**, *489*, 584–594. https://doi.org/10.1016/j.apsusc.2019.05.314.
42. Chieregato, F.; Molinari, A.; Milani, M.; Fendrich, M.; Orlandi, M.; Miotello, A. Colloids and Surfaces A : Physicochemical and Engineering Aspects An immobilized iron-oxides catalytic platform for photocatalysis and photosynthesis : Visible light induced hydroxylation reactions. *Colloids Surf. A Physicochem. Eng. Asp.* **2022**, *648*, 129428. https://doi.org/10.1016/j.colsurfa.2022.129428.
43. Orlandi, M.; Filosa, N.; Bettonte, M.; Fendrich, M.; Girardini, M.; Battistini, T.; Miotello, A. Treatment of surfactant-rich industrial wastewaters with concentrated sunlight: Toward solar wastewater remediation. *Int. J. Environ. Sci. Technol.* **2019**, *16*, 2109–2114. https://doi.org/10.1007/s13762-018-2099-7.
44. Phillips, G.; Johnson, B.E.; Ferguson, J. The loss of antibiotic activity of ciprofloxacin by photodegradation. *J. Antimicrob. Chemother.* **1990**, *26*, 783–789. https://doi.org/10.1093/jac/26.6.783.
45. Karim, A.V.; Shriwastav, A. Degradation of ciprofloxacin using photo, sono, and sonophotocatalytic oxidation with visible light and low-frequency ultrasound: Degradation kinetics and pathways. *Chem. Eng. J.* **2020**, *392*, 124853. https://doi.org/10.1016/j.cej.2020.124853.
46. Rashid, J.; Abbas, A.; Chang, L.C.; Iqbal, A.; Haq, I.U.; Rehman, A.; Awan, S.U.; Arshad, M.; Rafique, M.; Barakat, M.A. Butterfly cluster like lamellar BiOBr/TiO_2 nanocomposite for enhanced sunlight photocatalytic mineralization of aqueous ciprofloxacin. *Sci. Total Environ.* **2019**, *665*, 668–677. https://doi.org/10.1016/j.scitotenv.2019.02.145.
47. Wagner, D.R.; Ament, K.; Mayr, L.; Martin, T.; Bloesser, A.; Schmalz, H.; Marschall, R.; Wagner, F.E.; Breu, J. Terrestrial solar radiation driven photodecomposition of ciprofloxacin in clinical wastewater applying mesostructured iron(III) oxide. *Environ. Sci. Pollut. Res.* **2021**, *28*, 6222–6231. https://doi.org/10.1007/s11356-020-10899-6.
48. Rajiv, P.; Mengelizadeh, N.; McKay, G.; Balarak, D. Photocatalytic degradation of ciprofloxacin with Fe_2O_3 nanoparticles loaded on graphitic carbon nitride: Mineralisation, degradation mechanism and toxicity assessment. *Int. J. Environ. Anal. Chem.* **2023**, *103*, 2193–2207. https://doi.org/10.1080/03067319.2021.1890059.

49. Wang, Y.; Li, X.; Lei, W.; Zhu, B.; Yang, J. Novel carbon quantum dot modified g-C_3N_4 nanotubes on carbon cloth for efficient degradation of ciprofloxacin. *Appl. Surf. Sci.* **2021**, *559*, 149967. https://doi.org/10.1016/j.apsusc.2021.149967.
50. Bonelli, M.; Cestari, C.; Miotello, A. Pulsed laser deposition apparatus for applied research. *Meas. Sci. Technol.* **1999**, *10*, 27–30. https://doi.org/10.1088/0957-0233/10/3/024.
51. Svoboda, L.; Praus, P.; Lima, M.J.; Sampaio, M.J.; Matýsek, D.; Ritz, M.; Dvorský, R.; Faria, J.L.; Silva, C.G. Graphitic carbon nitride nanosheets as highly efficient photocatalysts for phenol degradation under high-power visible LED irradiation. *Mater. Res. Bull.* **2018**, *100*, 322–332. https://doi.org/10.1016/j.materresbull.2017.12.049.
52. Zhang, Y.; Pan, Q.; Chai, G.; Liang, M.; Dong, G.; Zhang, Q.; Qiu, J. Synthesis and luminescence mechanism of multicolor-emitting g-C_3N_4 nanopowders by low temperature thermal condensation of melamine. *Sci. Rep.* **2013**, *3*, 1943. https://doi.org/10.1038/srep01943.
53. Jiang, J.; Zou, J.; Wee, A.T.S.; Zhang, W. Use of single-layer g-C_3N_4/Ag hybrids for surface-enhanced raman scattering (SERS). *Sci. Rep.* **2016**, *6*, 34599. https://doi.org/10.1038/srep34599.
54. Mishra, D.; Arora, R.; Lahiri, S.; Amritphale, S.S.; Chandra, N. Synthesis and characterization of iron oxide nanoparticles by solvothermal method. *Prot. Met. Phys. Chem. Surf.* **2014**, *50*, 628–631. https://doi.org/10.1134/S2070205114050128.
55. Ristić, M.; De Grave, E.; Musić, S.; Popović, S.; Orehovec, Z. Transformation of low crystalline ferrihydrite to α-Fe_2O_3 in the solid state. *J. Mol. Struct.* **2007**, *834–836*, 454–460. https://doi.org/10.1016/j.molstruc.2006.10.016.
56. Soler, M.A.G.; Qu, F. *Raman Spectroscopy of Iron Oxide Nanoparticles BT—Raman Spectroscopy for Nanomaterials Characterization*; Kumar, C.S.S.R., Ed.; Springer: Berlin/Heidelberg, Germany, 2012; pp. 379–416; ISBN 978-3-642-20620-7.
57. Zhang, Z.; Huang, J.; Yuan, Q.; Dong, B. Intercalated graphitic carbon nitride: A fascinating two-dimensional nanomaterial for an ultra-sensitive humidity nanosensor. *Nanoscale* **2014**, *6*, 9250–9256. https://doi.org/10.1039/c4nr01570c.
58. Shi, Q.; Huang, J.; Yang, Y.; Wu, J.; Shen, J.; Liu, X.; Sun, A.; Liu, Z. In-situ construction of urchin-like hierarchical g-C_3N_4/NiAl-LDH hybrid for efficient photoreduction of CO_2. *Mater. Lett.* **2020**, *268*, 127560. https://doi.org/10.1016/j.matlet.2020.127560.
59. Ding, Q.; Lam, F.L.Y.; Hu, X. Complete degradation of ciprofloxacin over g-C_3N_4-iron oxide composite via heterogeneous dark Fenton reaction. *J. Environ. Manag.* **2019**, *244*, 23–32. https://doi.org/10.1016/j.jenvman.2019.05.035.
60. Liu, L.; Wang, M.; Wang, C. In-situ synthesis of graphitic carbon nitride/iron oxide−copper composites and their application in the electrochemical detection of glucose. *Electrochim. Acta* **2018**, *265*, 275–283. https://doi.org/10.1016/j.electacta.2018.01.149.
61. Wang, X.; Han, D.; Ding, Y.; Liu, J.; Cai, H.; Jia, L.; Cheng, X.; Wang, J.; Fan, X. A low-cost and high-yield approach for preparing g-C_3N_4 with a large specific surface area and enhanced photocatalytic activity by using formaldehyde-treated melamine. *J. Alloys Compd.* **2020**, *845*, 156293. https://doi.org/10.1016/j.jallcom.2020.156293.
62. Wang, S.; Meng, C.; Bai, Y.; Wang, Y.; Liu, P.; Pan, L.; Zhang, L.; Yin, Z.; Tang, N. Synergy Promotion of Elemental Doping and Oxygen Vacancies in Fe_2O_3 Nanorods for Photoelectrochemical Water Splitting. *ACS Appl. Nano Mater.* **2022**, *5*, 6781–6791. https://doi.org/10.1021/acsanm.2c00777.
63. Yamashita, T.; Hayes, P. Analysis of XPS spectra of Fe^{2+} and Fe^{3+} ions in oxide materials. *Appl. Surf. Sci.* **2008**, *254*, 2441–2449. https://doi.org/10.1016/j.apsusc.2007.09.063.
64. Guo, C.; Xia, F.; Wang, Z.; Zhang, L.; Xi, L.; Zuo, Y. Flowerlike iron oxide nanostructures and their application in microwave absorption. *J. Alloys Compd.* **2015**, *631*, 183–191. https://doi.org/10.1016/j.jallcom.2015.01.087.
65. Wang, W.; Zhang, H.; Zhang, S.; Liu, Y.; Wang, G.; Sun, C.; Zhao, H. Potassium-Ion-Assisted Regeneration of Active Cyano Groups in Carbon Nitride Nanoribbons: Visible-Light-Driven Photocatalytic Nitrogen Reduction. *Angew. Chem. Int. Ed.* **2019**, *58*, 16644–16650. https://doi.org/10.1002/anie.201908640.
66. Zhang, J.-R.; Ma, Y.; Wang, S.-Y.; Ding, J.; Gao, B.; Kan, E.; Hua, W. Accurate K-edge X-ray photoelectron and absorption spectra of g-C_3N_4 nanosheets by first-principles simulations and reinterpretations. *Phys. Chem. Chem. Phys.* **2019**, *21*, 22819–22830. https://doi.org/10.1039/C9CP04573B.
67. Nikolaev, V.; Sladkevich, S.; Divina, U.; Prikhodchenko, P.V.; Gasser, G.; Falciola, L.; Longhi, M.; Lev, O. LC-MS analysis of nitroguanidine compounds by catalytic reduction using palladium modified graphitic carbon nitride catalyst. *Microchim. Acta* **2021**, *188*, 152. https://doi.org/10.1007/s00604-021-04814-0.
68. Shen, L.; Xing, Z.; Zou, J.; Li, Z.; Wu, X.; Zhang, Y.; Zhu, Q.; Yang, S.; Zhou, W. Black TiO_2 nanobelts/g-C_3N_4 nanosheets Laminated Heterojunctions with Efficient Visible-Light-Driven Photocatalytic Performance. *Sci. Rep.* **2017**, *7*, 41978. https://doi.org/10.1038/srep41978.
69. Xu, Y.; Huang, S.; Xie, M.; Li, Y.; Xu, H.; Huang, L.; Zhang, Q.; Li, H. Magnetically separable Fe_2O_3/g-C_3N_4 catalyst with enhanced photocatalytic activity. *RSC Adv.* **2015**, *5*, 95727–95735. https://doi.org/10.1039/c5ra18009k.
70. Yi, S.S.; Wulan, B.R.; Yan, J.M.; Jiang, Q. Highly Efficient Photoelectrochemical Water Splitting: Surface Modification of Cobalt-Phosphate-Loaded Co_3O_4/Fe_2O_3 p–n Heterojunction Nanorod Arrays. *Adv. Funct. Mater.* **2019**, *29*, 1801902. https://doi.org/10.1002/adfm.201801902.
71. McIntyre, N.S.; Zetaruk, D.G. X-ray photoelectron spectroscopic studies of iron oxides. *Anal. Chem.* **1977**, *49*, 1521–1529. https://doi.org/10.1021/ac50019a016.
72. Grosvenor, A.P.; Kobe, B.A.; Biesinger, M.C.; McIntyre, N.S. Investigation of multiplet splitting of Fe 2p XPS spectra and bonding in iron compounds. *Surf. Interface Anal.* **2004**, *36*, 1564–1574. https://doi.org/10.1002/sia.1984.
73. Zhao, L.; Guo, L.; Tang, Y.; Zhou, J.; Shi, B. Novel g-C_3N_4/C/Fe_2O_3 Composite for Efficient Photocatalytic Reduction of Aqueous Cr(VI) under Light Irradiation. *Ind. Eng. Chem. Res.* **2021**, *60*, 13594–13603. https://doi.org/10.1021/acs.iecr.1c02411.

74. Carbajo, J.; Silveira, J.E.; Pliego, G.; Zazo, J.A.; Casas, J.A. Increasing Photo-Fenton process Efficiency: The effect of high temperatures. *Sep. Purif. Technol.* **2021**, *271*, 118876. https://doi.org/10.1016/j.seppur.2021.118876.
75. Yadav, M.; Yadav, A.; Fernandes, R.; Popat, Y.; Orlandi, M.; Dashora, A.; Kothari, D.C.; Miotello, A.; Ahuja, B.L.; Patel, N. Tungsten-doped TiO_2/reduced Graphene Oxide nano-composite photocatalyst for degradation of phenol: A system to reduce surface and bulk electron-hole recombination. *J. Environ. Manag.* **2017**, *203*, 364–374. https://doi.org/10.1016/j.jenvman.2017.08.010.
76. He, W.; Jia, H.; Li, Z.; Miao, C.Q.; Lu, R.; Zhang, S.; Zhang, Z. Magnetic recyclable g-C_3N_4/Fe_3O_4@MIL-100(Fe) ternary catalyst for photo-Fenton degradation of ciprofloxacin. *J. Environ. Chem. Eng.* **2022**, *10*, 108698. https://doi.org/10.1016/j.jece.2022.108698.
77. Liu, Y.; Yu, Y.X.; Zhang, W. De Photoelectrochemical study on charge transfer properties of nanostructured Fe_2O_3 modified by g-C_3N_4. *Int. J. Hydrogen Energy* **2014**, *39*, 9105–9113. https://doi.org/10.1016/j.ijhydene.2014.03.248.
78. Van Pham, V.; Truong, T.K.; Hai, L.V.; La, H.P.P.; Nguyen, H.T.; Lam, V.Q.; Tong, H.D.; Nguyen, T.Q.; Sabbah, A.; Chen, K.-H.; et al. S-Scheme α-Fe_2O_3/g-C_3N_4 Nanocomposites as Heterojunction Photocatalysts for Antibiotic Degradation. *ACS Appl. Nano Mater.* **2022**, *5*, 4506–4514. https://doi.org/10.1021/acsanm.2c00741.
79. Danish, M.; Saud Athar, M.; Ahmad, I.; Warshagha, M.Z.A.; Rasool, Z.; Muneer, M. Highly efficient and stable Fe_2O_3/g-C_3N_4/GO nanocomposite with Z-scheme electron transfer pathway: Role of photocatalytic activity and adsorption isotherm of organic pollutants in wastewater. *Appl. Surf. Sci.* **2022**, *604*, 154604. https://doi.org/10.1016/j.apsusc.2022.154604.
80. Wang, J.; Zuo, X.; Cai, W.; Sun, J.; Ge, X.; Zhao, H. Facile fabrication of direct solid-state Z-scheme g-C_3N_4/Fe_2O_3 heterojunction: A cost-effective photocatalyst with high efficiency for the degradation of aqueous organic pollutants. *Dalton Trans.* **2018**, *47*, 15382–15390. https://doi.org/10.1039/c8dt02893a.
81. Li, X.; Qiu, Y.; Zhu, Z.; Chen, T.; Zhang, H.; Yin, D. Construction of magnetically separable dual Z-scheme g-C_3N_4/α-Fe_2O_3/Bi_3TaO_7 photocatalyst for effective degradation of ciprofloxacin under visible light. *Chem. Eng. J.* **2022**, *440*, 135840. https://doi.org/10.1016/j.cej.2022.135840.
82. Shen, Y.; Han, Q.; Hu, J.; Gao, W.; Wang, L.; Yang, L.; Gao, C.; Shen, Q.; Wu, C.; Wang, X.; et al. Artificial Trees for Artificial Photosynthesis: Construction of Dendrite-Structured α-Fe_2O_3/g-C_3N_4 Z-Scheme System for Efficient CO_2 Reduction into Solar Fuels. *ACS Appl. Energy Mater.* **2020**, *3*, 6561–6572. https://doi.org/10.1021/acsaem.0c00750.
83. Zhou, L.; Wang, L.; Zhang, J.; Lei, J.; Liu, Y. Well-Dispersed Fe_2O_3 Nanoparticles on g-C_3N_4 for Efficient and Stable Photo-Fenton Photocatalysis under Visible-Light Irradiation. *Eur. J. Inorg. Chem.* **2016**, *2016*, 5387–5392. https://doi.org/10.1002/ejic.201600959.
84. Liu, D.; Li, C.; Ni, T.; Gao, R.; Ge, J.; Zhang, F.; Wu, W.; Li, J.; Zhao, Q. 3D interconnected porous g-C_3N_4 hybridized with Fe_2O_3 quantum dots for enhanced photo-Fenton performance. *Appl. Surf. Sci.* **2021**, *555*, 149677. https://doi.org/10.1016/j.apsusc.2021.149677.
85. Zhao, H.; Tian, C.; Mei, J.; Yang, S.; Wong, P.K. Faster electron injection and higher interface reactivity in g-C_3N_4/Fe_2O_3 nanohybrid for efficient photo-Fenton-like activity toward antibiotics degradation. *Environ. Res.* **2021**, *195*, 110842. https://doi.org/10.1016/j.envres.2021.110842.
86. Guo, T.; Wang, K.; Zhang, G.; Wu, X. A novel α-Fe_2O_3@g-C_3N_4 catalyst: Synthesis derived from Fe-based MOF and its superior photo-Fenton performance. *Appl. Surf. Sci.* **2019**, *469*, 331–339. https://doi.org/10.1016/j.apsusc.2018.10.183.
87. Ge, F.; Li, X.; Wu, M.; Ding, H.; Li, X. A type II heterojunction α-Fe_2O_3/g-C_3N_4 for the heterogeneous photo-Fenton degradation of phenol. *RSC Adv.* **2022**, *12*, 8300–8309. https://doi.org/10.1039/d1ra09282k.
88. Huang, Y.; Chen, B.; Duan, J.; Yang, F.; Wang, T.; Wang, Z.; Yang, W.; Hu, C.; Luo, W.; Huang, Y. Graphitic Carbon Nitride (g-C3N4): An Interface Enabler for Solid-State Lithium Metal Batteries. *Angew. Chemie Int. Ed.* **2020**, *59*, 3699–3704. https://doi.org/https://doi.org/10.1002/anie.201914417.
89. Liu, X.; Yang, W.; Chen, L.; Liu, Z.; Long, L.; Wang, S.; Liu, C.; Dong, S.; Jia, J. Graphitic Carbon Nitride (g-C3N4)-Derived Bamboo-Like Carbon Nanotubes/Co Nanoparticles Hybrids for Highly Efficient Electrocatalytic Oxygen Reduction. *ACS Appl. Mater. Interfaces* **2020**, *12*, 4463–4472. https://doi.org/10.1021/acsami.9b18454.
90. Ong, W.-J.; Tan, L.-L.; Ng, Y.H.; Yong, S.-T.; Chai, S.-P. Graphitic Carbon Nitride (g-C3N4)-Based Photocatalysts for Artificial Photosynthesis and Environmental Remediation: Are We a Step Closer to Achieving Sustainability? *Chem. Rev.* **2016**, *116*, 7159–7329. https://doi.org/10.1021/acs.chemrev.6b00075.
91. Wang, Y.; Zhang, X.; Ding, X.; Li, Y.; Wu, B.; Zhang, P.; Zeng, X.; Zhang, Q.; Du, Y.; Gong, Y.; Zheng, K.; Tian, X. Stitching Graphene Sheets with Graphitic Carbon Nitride: Constructing a Highly Thermally Conductive rGO/g-C3N4 Film with Excellent Heating Capability. *ACS Appl. Mater. Interfaces* **2021**, *13*, 6699–6709. https://doi.org/10.1021/acsami.0c22057.
92. Qu, Y.; Li, X.; Zhang, H.; Huang, R.; Qi, W.; Su, R.; He, Z. Controllable synthesis of a sponge-like Z-scheme N,S-CQDs/Bi_2MoO_6@TiO_2 film with enhanced photocatalytic and antimicrobial activity under visible/NIR light irradiation. *J. Hazard. Mater.* **2022**, *429*, 128310. https://doi.org/10.1016/j.jhazmat.2022.128310.
93. Masekela, D.; Hintsho-Mbita, N.C.; Mabuba, N. Application of a piezo-photocatalytic thin film (FTO/$BaTiO_3$/SnO_2) for enhanced degradation of organic pollutants and disinfection of wastewater. *Ceram. Int.* **2023**, *49*, 7566–7579. https://doi.org/10.1016/j.ceramint.2022.10.251.
94. Gómez, E.; Cestaro, R.; Philippe, L.; Serrà, A. Electrodeposition of nanostructured Bi_2MoO_6@Bi_2MoO_{6-x} homojunction films for the enhanced visible-light-driven photocatalytic degradation of antibiotics. *Appl. Catal. B Environ.* **2022**, *317*, 121703. https://doi.org/10.1016/j.apcatb.2022.121703.

95. Triquet, T.; Tendero, C.; Latapie, L.; Manero, M.H.; Richard, R.; Andriantsiferana, C. TiO_2 MOCVD coating for photocatalytic degradation of ciprofloxacin using 365 nm UV LEDs—Kinetics and mechanisms. *J. Environ. Chem. Eng.* **2020**, *8*, 104544. https://doi.org/10.1016/j.jece.2020.104544.
96. Tantis, I.; Bousiakou, L.; Karikas, G.A.; Lianos, P. Photocatalytic and photoelectrocatalytic degradation of the antibacterial agent ciprofloxacin. *Photochem. Photobiol. Sci.* **2015**, *14*, 603–607. https://doi.org/10.1039/c4pp00377b.
97. Lima, A.S.; Rocha, R.D.C.; Pereira, E.C.; Sikora, M. de S. Photodegradation of Ciprofloxacin antibiotic over TiO_2 grown by PEO: Ecotoxicity response in *Lactuca sativa* L. and *Lemna minor*. *Int. J. Environ. Sci. Technol.* **2022**, *19*, 2771–2780. https://doi.org/10.1007/s13762-021-03239-9.
98. Kumar, J.V.; Karthik, R.; Chen, S.M.; Muthuraj, V.; Karuppiah, C. Fabrication of potato-like silver molybdate microstructures for photocatalytic degradation of chronic toxicity ciprofloxacin and highly selective electrochemical detection of H_2O_2. *Sci. Rep.* **2016**, *6*, 34149. https://doi.org/10.1038/srep34149.
99. Mirzai, M.; Akhlaghian, F.; Rahmani, F. Photodegradation of ciprofloxacin in water using photocatalyst of zinc oxide nanowires doped with copper and cerium oxides. *Water Environ. J.* **2020**, *34*, 420–431. https://doi.org/10.1111/wej.12477.
100. Marshall, C.P.; Dufresne, W.J.B.; Rufledt, C.J. Polarized Raman spectra of hematite and assignment of external modes. *J. Raman Spectrosc.* **2020**, *51*, 1522–1529. https://doi.org/https://doi.org/10.1002/jrs.5824.
101. Tonda, S.; Kumar, S.; Kandula, S.; Shanker, V. Fe-doped and -mediated graphitic carbon nitride nanosheets for enhanced photocatalytic performance under natural sunlight. *J. Mater. Chem. A* **2014**, *2*, 6772–6780. https://doi.org/10.1039/C3TA15358D.
102. Meier, R.J.; Maple, J.R.; Hwang, M.-J.; Hagler, A.T. Molecular Modeling Urea- and Melamine-Formaldehyde Resins. 1. A Force Field for Urea and Melamine. *J. Phys. Chem.* **1995**, *99*, 5445–5456. https://doi.org/10.1021/j100015a030.
103. Jelı, M.; Zemek, J.; Trchová, M.; Vorlı, V.; Lančok, J.; Tomov, R.; Šimečková, M. CNx films created by combined laser deposition and r.f. discharge: XPS, FTIR and Raman analysis. *Thin Solid Film.* **2000**, *366*, 69–76. https://doi.org/https://doi.org/10.1016/S0040-6090(00)00853-1.